Ore Geology Reviews 75 (2016) 52–75

Contents lists available at ScienceDirect

Ore Geology Reviews

journal homepage: www.elsevier.com/locate/oregeorev

Synmetamorphic Cu remobilization during the Pan-African orogeny: Microstructural, petrological and geochronological data on the kyanite-micaschists hosting the Cu(–U) Lumwana deposit in the Western Zambian Copperbelt of the Lufilian belt

François Turlin [a,*], Aurélien Eglinger [a,1], Olivier Vanderhaeghe [a,2], Anne-Sylvie André-Mayer [a], Marc Poujol [b], Julien Mercadier [a], Ryan Bartlett [c]

[a] GeoRessources Lab., Université de Lorraine, CNRS, CREGU, Campus Aiguillettes, Faculté des Sciences et Technologies, rue Jacques Callot, Vandoeuvre-lès-Nancy, F-54506, France
[b] Géosciences Rennes, UMR 6118, Université de Rennes 1, 35042 Rennes Cedex, France
[c] Barrick Limited, Lumwana, Zambia

ARTICLE INFO

Article history:
Received 14 June 2015
Received in revised form 10 November 2015
Accepted 15 November 2015
Available online 17 November 2015

Keywords:
Copper
Amphibolite facies
U–Th–Pb geochronology
Pan-African orogeny
Syn-tectonic mineralization

ABSTRACT

The Pan-African Lufilian orogenic belt hosts world-class Cu deposits. In the Congolese Copperbelt (DRC), Cu(–Co) deposits, are mostly hosted within evaporitic and siliciclastic Neoproterozoic metasedimentary rocks (Mines Subgroup) and are interpreted as syn- to late-diagenetic deposits. In this paper, we present new data on Cu(–U) deposit hosted in metamorphic rocks of the internal zone of the Lufilian belt known as the Western Zambian Copperbelt in which a primary Cu mineralization is overprinted by a second syn-metamorphic Cu mineralizing event. This mineralizing event is synchronous with the Pan-African metamorphism affecting both the pre-Katanga basement and the Katanga metasedimentary sequence. Cu(–U) occurrences in the Western Zambian Copperbelt are hosted by kyanite-micaschists metamorphosed in the upper amphibolite facies.

Mineral inclusions of graphite, micas and sulfides in kyanite porphyroblasts of the Cu-bearing kyanite-micaschists in the Lumwana Cu deposit point to a sedimentary protolith with relics of an inherited Cu stock. Based on petrologic, microstructural and geochronological evidence, we propose that this initial Cu-stock was remobilized during the Pan-African orogeny. Graphite, micas and sulfides preserved in a first generation of kyanite poikiloblasts (Ky_1) define an inherited $S_{0/1}$ foliation developed during the prograde part of the *P–T* path (D_1 deformation-metamorphic stage) reaching HP–MT metamorphic conditions.

Remobilization during the retrograde part of the *P–T* path is evidenced by chalcopyrite–pyrrhotite and chalcopyrite–bornite delineating a steep-dipping S_2 schistosity and by chalcopyrite and bornite delineating a shallow-dipping S_3 schistosity associated with top to the south kinematic criteria. This retrograde path is coeval with ductile deformation in the kyanite field as evidenced by a second generation of synkinematic kyanite porphyroblasts (Ky_2) transposed in the S_3 schistosity (Ky_{2-3}), and is marked by progressive cooling from ca. 620 °C down to 580 °C (rutile geothermometry). Syn-S_{2-3} metamorphic monazite grains yield U–Th–Pb ages ranging from ca. 540 to 500 Ma.

Final retrogression and remobilization of Cu is marked by recrystallization of the sulfides in top to the north C_3 shear bands associated with rutile crystals yielding temperatures from ca. 610 to 540 °C. This final remobilization is younger than ca. 500 Ma (youngest U–Th–Pb age on syn-S_3 recrystallized monazite). These data are consistent with successive Cu remobilization for more than 40 Ma during Pan-African reworking of sediment-hosted deposits either from the basement of the Katanga sedimentary sequence or from the Katanga sequence itself marked by burial (D_1), syn-orogenic exhumation (D_2), and post-orogenic exhumation during gravitational collapse (D_3).

* Corresponding author at: Université de Lorraine, CNRS, CREGU, GeoRessources Lab., Campus Aiguillettes, Faculté des Sciences et Technologies, rue Jacques Callot, Vandœuvre-lès-Nancy, F-54506, France.
E-mail address: francois.turlin@univ-lorraine.fr (F. Turlin).
[1] Now at Chrono-Environnement, UMR 6249, CNRS, Université de Franche-Comté, 16 rue de Gray, 25030 Besançon, France.
[2] Now at Géosciences Environnement Toulouse, UMR 5563, Université de Toulouse, France.

http://dx.doi.org/10.1016/j.oregeorev.2015.11.022
0169-1368/

1. Introduction

Cu deposits are hosted by a wide variety of rocks including sedimentary, metamorphic and magmatic rocks (Dill, 2010 and references therein). Among them, sediment-hosted stratiform Cu deposits represent around 25% of the Cu production at a mean grade of 2.4% (Hitzman et al., 2005; Selley et al., 2005). The Lufilian orogenic belt (Fig. 1), straddling the border between the Democratic Republic of Congo (DRC) and Zambia, formed during the Pan-African orogenic cycle and contains the largest sediment-hosted stratiform Cu province in the world, the Central African Copperbelt (Cailteux et al., 2005; Muchez et al., 2015; Selley et al., 2005).

This Neoproterozoic belt is mainly divided into two tectono-metamorphic zones from north to south (De Swardt and Drysdall, 1964): (i) the External fold-and-thrust belt in the north and (ii) the Domes region (in the south of and on the border between DRC and Zambia, Fig. 1). The External fold-and-thrust belt, with metamorphism not exceeding greenschist facies (Fig. 1, Key et al., 2001; Torremans et al., 2013) contains (i) Cu–Co (e.g. Kamoto, El Desouky et al., 2009; Muchez et al., 2008, 2015) and Pb–Zn–Cu deposits (e.g. Kipushi, Batumike et al., 2007; Kamona et al., 1999; Kampunzu et al., 2009) defining the Congolese Copperbelt (Selley et al., 2005), and (ii) Cu–Co deposits around the Kafue Anticline (e.g. Konkola, Nchanga, Selley et al., 2005) designated as the Eastern Zambian Copperbelt. The Domes region, also known as the Western Zambian Copperbelt (Selley et al., 2005), contains Cu–Co deposits (e.g. Lumwana, Bernau, 2007; Bernau et al., 2013; Nowecki, 2014) and Co–Ni–Cu (e.g. Kalumbila, Capistrant et al., 2015; Steven and Armstrong, 2003), around domes cored by gneisses and migmatites (Fig. 1, Hitzman et al., 2012), recording the highest metamorphic *P–T* conditions (up to upper amphibolite facies, Bernau, 2007; Bernau et al., 2013; Cosi et al., 1992; Eglinger et al., 2014b, in press; John et al., 2004). These copper occurrences are locally associated with uranium mineral occurrences (Cosi et al., 1992; Decrée et al., 2011; Eglinger et al., 2013).

In the Congolese and Eastern Zambian Copperbelts, these deposits are hosted within the lower part of the Neoproterozoic Katanga metasedimentary sequence, the Roan (Mines Subgroup, e.g. Kamoto deposit, Fig. 2, Muchez et al., 2015) and Lower Roan Group (e.g. Konkola deposit, Fig. 2, Selley et al., 2005) respectively. In addition, recent studies brought geochronological evidence that the Cu mineralization in the

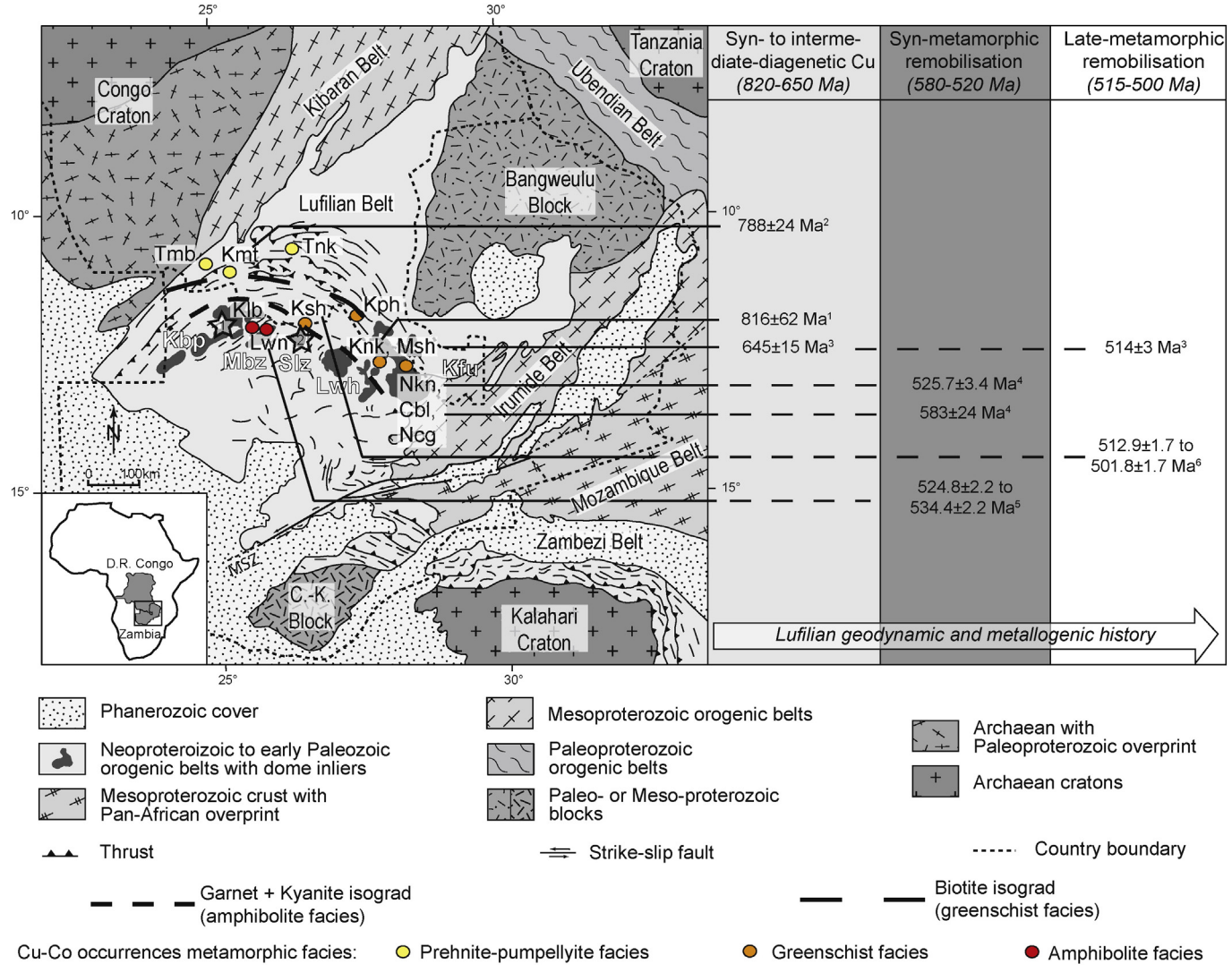

Fig. 1. Geological map of the Lufilian orogenic belt, metamorphic facies repartition and geochronological constraints available in the literature on Cu–Co occurrences and the interpreted geodynamic stage of their emplacement (modified after Eglinger et al., 2013). Lolwa and Mitukuluku uranium occurrences are represented as stars 1 and 2 respectively. Abbreviations: Cbl = Chibuluma West; Klb = Kalumbila; Knk = Konkola; Kmt = Kamoto; Kph = Kipushi; Ksh = Kansanshi; Lwn = Lumwana; Msh = Musoshi; Ncg = Nchanga; Nkn = Nkana-Mindola; Tmb = Tombolo; Tnk = Tenke. Kbp = Kabompo Dome; Mbz = Mwombezhi Dome; Slz = Solwezi Dome; Lwh = Luiswishi Dome; Kfu = Kafue Anticline; C.–K. = Choma–Kalomo Block; MSZ = Mwembeshi Shear Zone. [1] = Barra and Broughton, unpublished data in Selley et al., 2005; [2] = Muchez et al., 2015; [3] = Richards et al., 1988b; [4] = Barra et al., 2004; [5] = Nowecki, 2014; and [6] = Torrealday et al., 2000.

Congolese and Eastern Zambian Copperbelts' sediment-hosted stratiform deposits are multistage, from early- to intermediate-diagenetic dated between ca. 820 and 650 Ma (Barra and Broughton, unpublished data in Selley et al., 2005; Barra et al., 2004; Muchez et al., 2015; Richards et al., 1988b) to a remobilization during the Pan-African metamorphism, metasomatism and deformation between ca. 580 Ma and ca. 520 Ma (Barra et al., 2004; Brems et al., 2009; Cailteux et al., 2005, 2007; Dewaele et al., 2006; El Desouky et al., 2009; Muchez and Corbella, 2012; Muchez et al., 2015; Nowecki, 2014; Richards et al., 1988a, 1988b; Selley et al., 2005; Steven and Armstrong, 2003; Sweeney and Binda, 1994).

In contrast, the mineralization of the Lumwana deposit, located in the Western Zambian Copperbelt (Mwombezhi Dome, Figs. 1 and 3), is hosted by kyanite-micaschists, and its origin is debated. According to Bernau (2007) and Bernau et al. (2013), the kyanite-micaschists represent pre-Katanga gneiss attributed to the basement of the Katanga metasedimentary sequence, affected by pervasive metasomatic transformation coeval with the development of shear zones during the Pan-African orogeny. These authors propose a syn-metamorphic remobilization of a pre-existing sulfide stock present in the gneissic protolith, but they do not provide geochronological constraints and do not specify the nature of the protolith of the micaschists (sedimentary or magmatic). Benham et al. (1976) proposed a sedimentary origin of the Lumwana's kyanite-micaschists based on the presence of graphite and the abundance of Al-rich minerals (kyanite, muscovite and phlogopite). In the case of an ortho-derived protolith containing Cu sulfides, this Cu would probably have a magmatic origin and thus the metallogenic model for the Cu mineralization from the Lumwana deposit would be totally different from what is described for the Congolese and Eastern Zambian Copperbelts. A Cu-rich sedimentary protolith metamorphosed during the Pan-African orogeny, would imply that the Lumwana deposit has to be considered as a pre-Katanga or Katanga sediment-hosted stratiform Cu deposit metamorphosed to upper amphibolite facies conditions.

Accordingly, the Lufilian orogenic belt is a perfect natural laboratory to study the evolution of Cu mineralizations under different metamorphic conditions, from prehnite–pumpellyite to greenschist facies for sediment-hosted stratiform Cu deposits of the Congolese Copperbelt, to upper greenschist facies in the Eastern Zambian Copperbelt and to upper amphibolite conditions (e.g. Lumwana deposit) in the Western Zambian Copperbelt during a complete orogenic cycle involving the remobilization of a pre-existing basement and its sedimentary cover. The goal of the present study is to identify the nature of the host rocks of the Cu deposits in the Zambian Lufilian belt in order to elaborate a new mineral system for Cu deposition and remobilization. In particular, we propose a critical appraisal of the two models presented above for the formation and the timing of the Cu(–U) mineralization in the Western Zambian Copperbelt. In order to provide such information on both the timing and the processes that lead to these concentrations in this part of the Lufilian orogenic belt, we focus on the Lumwana deposit which is located along the margin of the Mwombezhi dome (Figs. 1 and 3). We had access to fresh samples from drilled cores thanks to the authorization of the Barrick Ltd. mining company. For this mineralization, we present: (i) a paragenetic sequence for the Cu(–U)-rich kyanite-micaschists and a structural interpretation of these metamorphosed lithologies; (ii) U–Th–Pb geochronological data on syn- to late-metamorphic monazite associated with Cu sulfides providing an age and a minimum constraint for the syn-metamorphic Cu mineralization of Lumwana and (iii) a model for the Lumwana deposit integrating the Cu mineral system in the tectonic evolution of the Pan-African orogeny in this part of the Lufilian belt.

2. Regional geology

The Lufilian orogenic belt extends for 700 km from east to west and for 150 km from north to south (Fig. 1). From north to south (present-day coordinates), this belt is divided into: (i) the External fold-and-thrust belt (designated in the present study as the Congolese Copperbelt), (ii) the Domes region (designated in the present study as the Zambian Copperbelt), (iii) the Synclinorial belt and (iv) the Katanga high (De Swardt and Drysdall, 1964; Porada and Berhorst, 2000). This orogenic belt is part of the Pan-African belts which formed during the

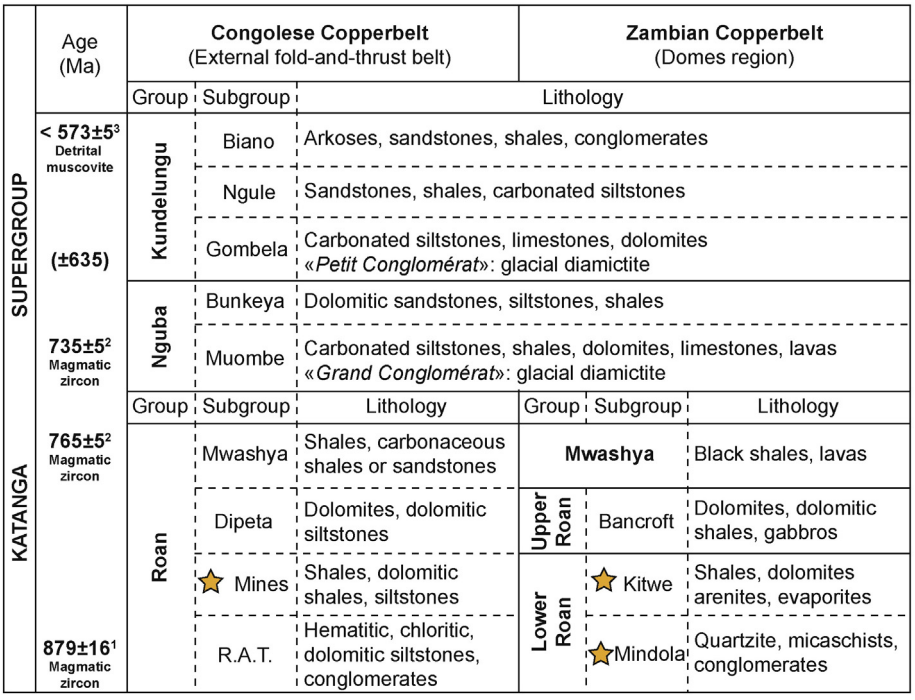

Fig. 2. Lithostratigraphy of the Katanga Supergroup in the Congolese Copperbelt (External fold-and-thrust belt) and in the Zambian Copperbelt (Domes Region) (modified after Eglinger et al., 2013). Stratigraphic position of Cu mineralization (yellow stars) is reported (Selley et al., 2005). Age constraints are provided by U-Pb dating on zircon grains from volcanic rocks ([1] = Hanson et al., 1994; [2] = Key et al., 2001) and by Ar–Ar thermochronology on detrital muscovite grains ([3] = Master et al., 2005). (For interpretation of the references to color in this figure legend, the reader is referred to the web version of this article.)

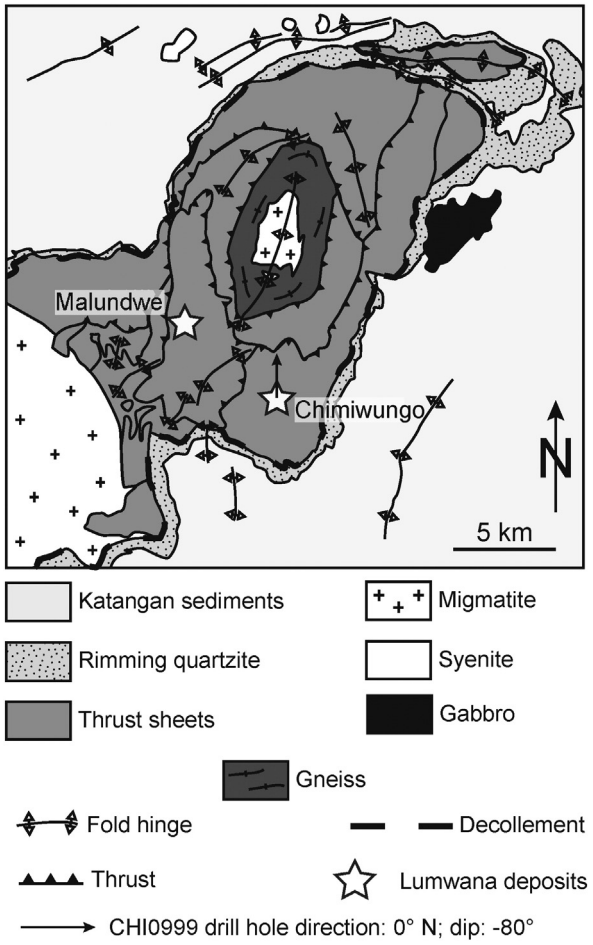

Fig. 3. Geological map of the Mwombezhi Dome, showing the location of the Malundwe deposit and Chimiwungo prospect, and the direction of the CHI0999 drilled core. Modified after Bernau (2007) and Bernau et al. (2013).

Neoproterozoic and early Paleozoic as a result of the collision between the Congo and Kalahari cratons that led to the formation of West Gondwana (Unrug, 1983; Porada and Berhorst, 2000; John et al., 2004).

2.1. Pan-African orogeny

Breakup of the Rodinia supercontinent was initiated at ca. 880 Ma (Hanson et al., 1994; Porada and Berhorst, 2000) as evidenced by the U–Pb ages obtained on magmatic zircon grains from the Kafue rhyolite and Nazingwe Formation volcanic rocks (880 ± 12 Ma and 880 ± 14 Ma respectively, Johnson et al., 2007) interpreted to record a period of continental rifting and opening of the Roan continental rift (Hanson et al., 1994; Porada and Berhorst, 2000; De Waele et al., 2008). The onset of the Lower Roan Group deposition occurred after intrusion, uplift and erosion of the youngest pre-Katanga intrusion in the Copperbelt basement, i.e. the calc-alkaline Nchanga granite, dated at 883 ± 10 Ma (U–Pb on magmatic zircon, Armstrong et al., 2005), as suggested by the presence of detrital zircon grains dated at ca. 880 Ma in a Lower Roan quartzite (Fig. 2, Armstrong et al., 2005) and its unconformity on top of the Nchanga granite. However, the youngest concordant analysis provides an upper limit for the deposition of the siliciclastic Roan sequence at 840 ± 13 Ma (Bartlett, pers. com.) in the Mwombezhi dome, Western Zambian Copperbelt.

A second rifting stage took place at ca. 750–720 Ma (Eglinger, 2013; Key et al., 2001) as indicated by the U–Pb ages obtained on magmatic zircon from lavas of the Mwashya Subgroup (Fig. 2, Key et al., 2001), and by U–Pb on zircon from meta-diorite intrusive within the Katanga sequence (Eglinger, 2013). This rifting stage led to the formation of an oceanic basin, at least in the Zambezi belt.

Subduction of the Zambezi ocean occurred between ca. 660 and 610 Ma (John et al., 2003) as recorded by eclogitic boudins (witness of the subduction phase between the Kalahari craton over-riding the Congo craton, John et al., 2003, 2004) within the Katanga sequence in the Zambezi belt, dated by a whole rock and garnet Lu–Hf isochron (John et al., 2004). The peak of metamorphism reached during continental collision is constrained by syn-metamorphic monazites from talc-kyanite-micaschists, described as whiteschists by Meneghel (1981). The syn-metamorphic monazites are dated between ca. 550 Ma and 530 Ma, obtained by U–Th–Pb dating (Eglinger et al., 2014b, in press) and U–Pb dating (John et al., 2004). The *P–T* constraints of these whiteschists are estimated at 13 ± 1 kbar and 750 ± 25 °C (Cosi et al., 1992; John et al., 2004).

Exhumation of these metamorphic rocks is evidenced by decompression and cooling recorded between ca. 510 and 470 Ma by Rb–Sr and K–Ar dating on biotite and muscovite from the basement and/or the metasedimentary cover (Cosi et al., 1992; John et al., 2004). In the Solwezi dome, monazite grains associated with the retrogression paragenesis of the kyanite-micaschists yield U–Th–Pb ages at ca. 510–500 Ma (Eglinger et al., 2014b, in press).

2.2. Metamorphic facies distribution

In the Congolese and Eastern Zambian Copperbelts, most, if not all (exception is e.g. Samba, Selley et al., 2005), of the deposits are hosted within the Lower Roan Group (<880 to ca. 790 Ma, Fig. 2, Selley, unpublished data in Hitzman et al., 2010), more precisely in the Mines Subgroup (Congolese Copperbelt)/Kitwe Subgroup (Zambian Copperbelt) (Fig. 2, Selley et al., 2005). A similar metasedimentary sequence is exposed in the Western Zambian Copperbelt, but this sequence was affected by higher *P–T* metamorphic conditions during the Pan-African orogeny. The metamorphic grade increases from prehnite-pumpellyite/lower greenschist facies in the Congolese Copperbelt (Fig. 1), to upper greenschist facies in the Eastern Zambian Copperbelt (Fig. 1) and to upper amphibolite facies in the Western Zambian Copperbelt (Fig. 1, Bernau, 2007; Bernau et al., 2013; Cosi et al., 1992; Eglinger et al., in press; Nowecki, 2014; Steven and Armstrong, 2003; Torremans et al., 2013).

2.3. Mwombezhi dome lithotectonic units and structures

The Zambian Copperbelt comprises a complexly folded nappe pile composed of Neoproterozoic metasediments and migmatitic gneisses. The latter structures are interpreted as basement cored nappes (Cosi et al., 1992; John et al., 2004). The Mwombezhi dome's core is composed of migmatitic granitic gneisses comprising (i) metatexitic paragneisses and orthogneisses, and (ii) enclaves and boudins of garnet-bearing amphibolite (Figs. 2 and 4; Eglinger et al., in press). These are interpreted as representing pre-Katanga basement (Bernau, 2007; Bernau et al., 2013; Cosi et al., 1992; Eglinger, 2013; John et al., 2004). These units are separated from the surrounding metasediments by a kyanite-micaschists layer representing a major shear zone (Fig. 3; Bernau, 2007; Bernau et al., 2013; Cosi et al., 1992; Eglinger et al., in press; John et al., 2004).

3. Cu mineralization

This section presents the different stages of remobilization during the Lufilian orogenic cycle of the sediment-hosted Cu mineralization, based on the textures and ages published in the literature.

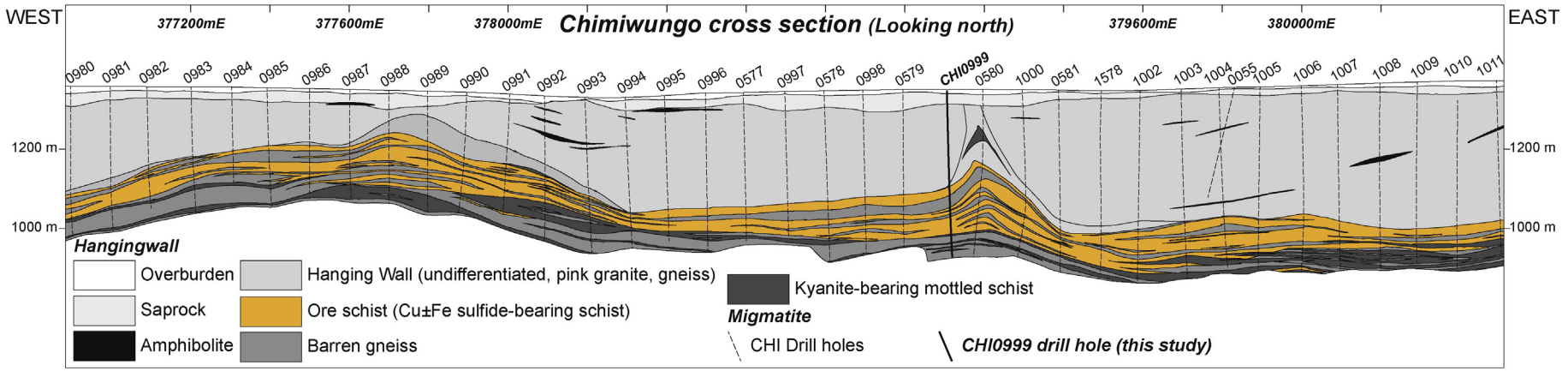

Fig. 4. Cross section across the Chimiwungo prospect (looking north) showing the position of drill cores, especially the CHI0999 sampled for the present study. Modified after the document 'Project Lumwana Chimiwungo Resource Drilling Validation' from Barrick Zambia.

3.1. Early- to intermediate-diagenetic Cu-mineralization

The Congolese and Eastern Zambian Copperbelts present framboidal pyrite and Cu sulfides attributed to an early- to intermediate-diagenetic (up to 180 °C) Cu-mineralization stage (Brems et al., 2009; Cailteux et al., 2005, 2007; Dewaele et al., 2006; El Desouky et al., 2009; Muchez et al., 2015; Richards et al., 1988a, 1988b; Selley et al., 2005; Steven and Armstrong, 2003; Sweeney and Binda, 1994). Sulfide crystallization is interpreted to be related to circulation of hydrothermal fluids during diagenesis and sulfur is assumed to result from bacterial sulfate reduction processes (El Desouky et al., 2009; Muchez et al., 2008). This hydrothermal diagenetic mineralization forms stratiform orebodies in siliciclastic or dolomitized metasedimentary rocks (Batumike et al., 2007; Cailteux et al., 2005; Dewaele et al., 2006). This mineralization stage is dated at:

- 816 ± 62 Ma by Re–Os dating on diagenetic chalcopyrite and bornite from Konkola (Eastern Zambian Copperbelt, Fig. 1, Barra and Broughton, unpublished data, in Selley et al., 2005);
- 788 ± 24 Ma by Re–Os dating on nodules or disseminated bornite from the Mines Subgroup (Fig. 2, Muchez et al., 2008, 2015) in Kamoto dolomite, dolomitic siltstone and shale, and silicified dolomite (Cailteux et al., 2005) (north of the Kabompo dome, Fig. 1);
- 645 ± 15 Ma by Pb–Pb dating on Cu–Fe sulfides (Richards et al., 1988b) in Musoshi ore shale (Eastern Zambian Copperbelt, Fig. 1).

These ages point to Cu-deposition between ca. 800 and 650 Ma, most probably around ca. 800 Ma as suggested by Re–Os ages, though it is not possible to argue whether this occurred in a single well-defined event or during a more prolonged episode (Muchez et al., 2015; Torremans et al., 2013).

3.2. Syn-metamorphic Cu- remobilization and mineralization

This stock of diagenetic sulfides (pyrite and Cu sulfides) is assumed (i) to be a major source for sulfur (Brems et al., 2009); and (ii) to have been replaced by Cu sulfides (chalcopyrite, bornite, digenite and chalcocite) during a syn-orogenic stage (≥200 °C up to ca. 450 °C) (Brems et al., 2009; Cailteux et al., 2005, 2007; Dewaele et al., 2006; El Desouky et al., 2009; Muchez et al., 2015; Muchez and Corbella, 2012; Richards et al., 1988a, 1988b; Selley et al., 2005; Steven and Armstrong, 2003; Sweeney and Binda, 1994). This mineralizing stage is evidenced in several Cu deposits such as Nkana-Mindola, Chibuluma West and Nchanga (Eastern Zambian Copperbelt, Fig. 1) where veinlets of bornite and chalcopyrite are hosted by argillite ± arenite metamorphosed in the greenschist facies and dated at 583 ± 24 Ma by Re–Os dating on chalcopyrite and bornite or carrollite (Barra et al., 2004; Selley et al., 2005). Molybdenite from Nkana-Mindola yields an age of 525.7 ± 3.4 Ma by Re–Os dating (Barra et al., 2004, Fig. 1), which is consistent with the peak of metamorphism recorded in the kyanite-micaschists at ca. 550–530 Ma (Eglinger et al., in press; John et al., 2004). In the Western Zambian Copperbelt (*P–T* metamorphic facies up to upper amphibolite facies, Bernau, 2007; Bernau et al., 2013; Cosi et al., 1992; Eglinger et al., 2013; John et al., 2004; Steven and Armstrong, 2003), the Lumwana Cu(–U) mineralization is hosted by kyanite-micaschists and is dated at: (i) 534.4 ± 2.2 Ma (granitic gneiss pegmatite), (ii) 534.2 ± 2.2 Ma (pegmatite vein), (iii) 525.9 ± 2.2 Ma (glassy quartz vein) and (iv) 524.8 ± 2.2 Ma (granitic gneiss) by Re–Os dating on syn-metamorphic molybdenite (Nowecki, 2014). These ages are interpreted by the author as dating Cu mineralization synchronous with the peak of metamorphism, even though the link between the dated samples and Cu sulfides from the kyanite-micaschists is not documented. Thus, in order to constrain the timing of syn-metamorphic Cu mineralization of the Western Zambian Copperbelt, it is required to bring new geochronological data.

The syn-metamorphic remobilization and ore crystallization are interpreted to be related to the circulation of metamorphic metal-rich brines (Cailteux et al., 2005; Dewaele et al., 2006; Eglinger et al., 2014b; McGowan et al., 2003, 2006). Meta-evaporites from the Roan Group are invoked as a potential source of the salt for these fluids (Fig. 2, Cailteux et al., 2005; Eglinger et al., 2013, 2014a, 2014b; El Desouky et al., 2009; Selley et al., 2005). This is consistent with the conclusions of McGowan et al. (2003, 2006) who proposed (i) a syn-orogenic circulation of metals transported by metals- and sulfates-bearing metamorphic fluids in Nchanga (Fig. 1) and (ii) the precipitation of sulfides related to the thermochemical sulfate reduction (TSR) of an ore-fluid, defined by the following reaction: $CaSO_4$ (anhydrite) + CH_4 (fluid) ⇔ $CaCO_3$ (calcite) + H_2S (fluid) + H_2O (fluid) (Cross, 1999; McGowan et al., 2003). This reaction requires an electron provider for the oxidation of sulfates during the redox process (Machel, 2001) which could be the organic matter initially present in the sediments.

3.3. Late-deformation Cu- remobilization and mineralization

In the Zambian Copperbelt, some Cu mineralization postdate the peak of metamorphism, i.e. are significantly younger than ca. 530 Ma (John et al., 2004; Eglinger et al., in press), and are thus related to the final stages of the tectonic evolution of the Lufilian belt (Brems et al., 2009; Richards et al., 1988b; Selley et al., 2005; Torrealday et al., 2000). The Musoshi mineralization (Fig. 1), dated at 645 ± 15 Ma (Richards et al., 1988a, 1988b; Selley et al., 2005), has been remobilized by hydrothermal fluids that lead to the formation of Cu-rich veins, and dated at 514 ± 2 Ma by U–Pb on rutile (Richards et al., 1988a) and at 514 ± 3 Ma by U–Pb on uraninite (Richards et al., 1988b). The Kansanshi deposit (Fig. 1) presents two generations of veins crosscutting the Katanga metasedimentary cover dated at: (i) 511.8 ± 1.7 Ma and 512.9 ± 1.7 Ma (first generation), and (ii) 503.0 ± 1.7 Ma and 501.8 ± 1.7 Ma (second generation) by Re–Os dating on molybdenite (Torrealday et al., 2000).

4. Sampling and analytical methods

4.1. Sampling of the micaschists

The present study focuses on the Lumwana deposit, located in the Western Zambian Copperbelt of the Lufilian belt and more precisely on the Mwombezhi Dome (Fig. 3). The CHI0999 drill-hole (East: 379109.8; North: 8641615; Elevation: 1355.413) from Chimiwungo (Barrick Ltd. prospect) was sampled (Fig. 4) and complemented by field investigations in the Mwombezhi dome area (Figs. 1 and 3) in April 2012. This drill-hole is representative of the mineralogy and microstructures developed in the Lumwana deposit and the chosen samples are similar to the ones investigated at the deposit scale in studies of Benham et al. (1976), Bernau (2007); Bernau et al. (2013) and Nowecki (2014). The drill-hole is located in the southern limb of the Mwombezhi dome and is plunging 80° towards the north. It comprises gneisses alternating with garnet- or kyanite-micaschists bearing Cu(–U) (Fig. 5). Three samples representative of the variety of the micaschists have been studied in detail. For each sample, the depth is indicated after the name of the drill-core (e.g.: CHI0999#88 for 88 m depth). One sample contains garnet but no kyanite nor Cu (CHI0999#88-13, Fig. 5); two samples do not contain garnet but bear kyanite and large Cu sulfides aggregates (CHI0999#89-16 and 93-17, Fig. 5). Sulfide assemblages differ from the top of the drill-core to the bottom. In the upper part, chalcopyrite is associated with pyrrhotite (CHI0999#89-16-a & 16-b, Fig. 5) while chalcopyrite is found together with bornite in the lower part (CHI0999#93-17-a & 17-b, Fig. 5).

The following analytical techniques were applied on grains positioned relative to the microstructure of the Cu-rich micaschists, i.e. the kyanite-micaschists, and on barren garnet-micaschists in order to

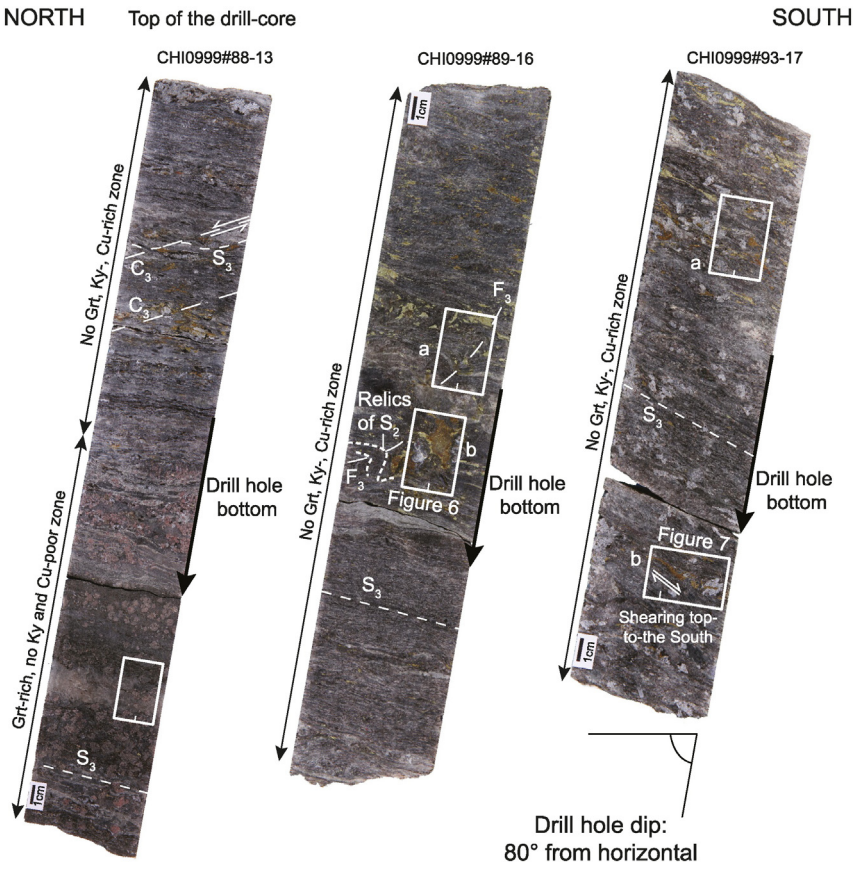

Fig. 5. Garnet or kyanite Cu-rich micaschists drill core samples CHI0999#88-13, 89-16 and 93-17 from Chimiwungo showing two metamorphic fabrics: S_2 schistosity attributed to D_2 metamorphic event, and S_3 and C_3 shear bands attributed to D_3 metamorphic event. Kyanite- and Cu-rich levels (chalcopyrite–pyrrhotite in samples CHI0999#88-13 and 89-16, and chalcopyrite–bornite in sample CHI0999#93-17) alternate with garnet-rich and Cu-poor levels. Kinematic indicators reveal a top to the south shear sense. White rectangles and associated letters indicate the position and name of thin sections. Abbreviations: Grt = garnet; Ky = kyanite.

constrain the different metamorphic and deformation stages recorded by these rocks.

4.2. Electron microprobe

Major elements were identified by the Electron Microprobe (EMP) method using a Cameca computer-controlled SX-100 (GeoRessources, Nancy). For silicates, the accelerating voltage was set at 15 kV, beam current at 12 nA and peak counting time varied from 10 to 20 s. For quantitative analyzes of monazite, the major and traces elements (P, Si, Ca, Y, La, Ce, Pr, Nd, Sm, Gd, Pb, Th, U) have been measured using an accelerating voltage of 20 kV, beam current was set to 100 nA. Peak counting time was set to 120 s for Pb, 100 s for U and 20 s for the others elements.

4.3. Laser Ablation-Inductively Coupled Plasma-Mass Spectrometry (LA-ICP-MS)

4.3.1. U–Th–Pb dating on monazite

U–Th–Pb geochronology of monazite grains from the kyanite-micaschists (samples CHI0999#93-17-a and -b) was conducted by in-situ (directly on thin sections) laser ablation inductively coupled plasma mass spectrometry (LA-ICP-MS) at Géosciences Rennes (France) using an ESI NWR193UC Excimer laser coupled to a quadripole Agilent 7700x ICP-MS.

During the course of an analysis, the signals of ^{204}(Pb + Hg), ^{206}Pb, ^{207}Pb, ^{208}Pb and ^{238}U masses are acquired. No common Pb correction was applied owing to the large isobaric interference with Hg. The ^{235}U signal is calculated from ^{238}U on the basis of the ratio ^{238}U/^{235}U = 137.88. Single analyzes consisted of 20 s of background integration followed by 60 s integration with the laser firing and then a 10 s delay to wash out the previous sample. For more information on the settings of the instrument, see Ballouard et al. (2015). Spot diameters of 15 μm associated with repetition rates of 3 Hz with a laser fluency of 7.3 J·cm^{-2} were used during the present study. Data were corrected for U–Pb and U–Th–Pb fractionation and for the mass bias by standard bracketing with repeated measurements of the Moacir monazite standard (Gasquet et al., 2010). Repeated analyzes of Manangoutry monazite standard (555.2 ± 4.3 Ma (MSWD = 1.6; n = 6); TIMS age 555 ± 2 Ma; Paquette and Tiepolo, 2007) treated as unknown were used to control the reproducibility and accuracy of the corrections. Data reduction was carried out with the GLITTER® software package developed by the Macquarie Research Ltd.. Concordia diagrams were generated using Isoplot/Ex (Ludwig, 2001). All errors given in Table 1 are listed at two sigma, but where data are combined to calculate weighted means, the final results are provided with 95% confidence limits.

4.3.2. Zr-in-rutile geothermometry

Cr (^{53}Cr), Zr (^{90}Zr and ^{91}Zr), and Nb (^{93}Nb) concentrations in rutile were quantified at GeoRessources (Nancy, France) using a laser ablation inductively coupled plasma mass spectrometry (LA-ICP-MS) system composed of a GeoLas excimer laser (ArF, 193 nm, Microlas) coupled to a conventional transmitted and reflected light microscope (Olympus BX51) for sample observation and laser beam focusing onto the sample and an Agilent 7500c quadrupole ICP-MS. The LA-ICP-MS system was optimized to have the highest sensitivity for all elements (from ^{7}Li to ^{238}U), ThO/Th ratio < 0.5% and Th/U ratio of 1. Samples were ablated with a 24 μm laser spot size, a fluence of 7.4 J·cm^{-2} and a pulse rate of 5 Hz. The carrier gas used was helium (0.5 l/min) which was mixed with argon (0.5 l/min) gas before entering the ICP-

Table 1
$^{208}Pb/^{232}Th$ monazite dating using LA-ICP-MS from samples CHI0999#93-17-a & -17-b.

Sample	Analysis no.	Concentrations/ppm				Isotopic ratios				Ages/Ma	
		Pb	Th	U	Th/U	$^{206}Pb/^{238}U$	2σ	$^{208}Pb/^{232}Th$	2σ	$^{208}Pb/^{232}Th$	2σ
CHI0999#93-17-a	1-1	893	26,664	4016	6.6	0.08311	0.00107	0.02563	0.00031	511.4	6.2
	1-2	1026	30,911	4494	6.9	0.08350	0.00107	0.02564	0.00031	511.6	6.2
	1-3	1305	41,223	5131	8.0	0.08348	0.00108	0.02552	0.00031	509.3	6.2
	1-4	924	28,083	3769	7.5	0.08436	0.00109	0.02613	0.00032	521.3	6.3
	1-5	736	20,945	3513	6.0	0.08461	0.00109	0.02622	0.00032	523.2	6.4
	1-6	872	23,901	3594	6.6	0.08491	0.00110	0.02652	0.00033	529.0	6.5
	1-7	896	23,679	3963	6.0	0.08491	0.00110	0.02672	0.00033	533.0	6.5
	2-1	1063	26,505	5309	5.0	0.08476	0.00110	0.02678	0.00033	534.2	6.5
	2-2	1073	29,815	4123	7.2	0.08563	0.00111	0.02693	0.00033	537.1	6.6
	2-3	897	20,691	5243	3.9	0.08521	0.00111	0.02635	0.00033	525.7	6.5
	2-4	859	23,603	3942	6.0	0.08357	0.00109	0.02595	0.00033	517.8	6.4
	2-5	843	23,118	3955	5.8	0.08303	0.00109	0.02586	0.00033	516.1	6.4
	3-1	968	27,701	4116	6.7	0.08211	0.00108	0.02601	0.00033	519.0	6.5
	3-2	856	24,584	3905	6.3	0.08123	0.00107	0.02535	0.00032	506.0	6.3
	4-1	1043	30,807	4108	7.5	0.08237	0.00108	0.02605	0.00033	519.7	6.5
	5-1	666	16,385	4142	4.0	0.08163	0.00108	0.02569	0.00033	512.8	6.4
	5-2	606	13,933	3907	3.6	0.08507	0.00112	0.02612	0.00033	521.1	6.5
	5-3	827	23,018	4297	5.4	0.08139	0.00108	0.02540	0.00032	507.0	6.4
	6-1	615	15,173	3924	3.9	0.08154	0.00108	0.02538	0.00032	506.6	6.4
	7-1	845	24,186	4264	5.7	0.08134	0.00108	0.02519	0.00032	502.8	6.3
	8-1	781	21,161	4159	5.1	0.08164	0.00109	0.02612	0.00034	521.1	6.6
	8-2	899	24,353	4688	5.2	0.08230	0.00110	0.02634	0.00034	525.5	6.7
	8-3	866	23,898	4492	5.3	0.08210	0.00110	0.02602	0.00034	519.2	6.6
	9-1	595	15,214	3478	4.4	0.08290	0.00111	0.02622	0.00034	523.2	6.7
	10-1	642	15,788	3984	4.0	0.08201	0.00110	0.02569	0.00033	512.8	6.6
	11-1	876	20,078	5799	3.5	0.08337	0.00112	0.02614	0.00034	521.5	6.7
	11-2	860	21,623	5039	4.3	0.08217	0.00111	0.02620	0.00034	522.8	6.7
	12-1	681	17,055	3974	4.3	0.08196	0.00111	0.02646	0.00034	527.8	6.8
CHI0999#93-17-b	1-1	2642	87,071	6599	13.2	0.08360	0.00112	0.02638	0.00035	526.2	6.9
	2-1	1941	60,195	6910	8.7	0.08236	0.00110	0.02572	0.00034	513.3	6.7
	3-1	1729	56,671	5206	10.9	0.08190	0.00109	0.02545	0.00034	508.0	6.6
	4-1	1751	52,087	6716	7.8	0.08324	0.00111	0.02597	0.00034	518.2	6.8
	4-2	1064	32,648	3934	8.3	0.08361	0.00112	0.02613	0.00035	521.3	6.8
	5-1	1300	40,675	4219	9.6	0.08485	0.00113	0.02645	0.00035	527.7	6.9
	5-2	1295	41,400	4366	9.5	0.08398	0.00112	0.02564	0.00034	511.8	6.6
	6-1	2151	71,100	5733	12.4	0.08205	0.00110	0.02636	0.00035	525.8	6.8
	6-2	1754	58,895	4464	13.2	0.08308	0.00111	0.02608	0.00034	520.3	6.7
	6-3	1079	34,137	3757	9.1	0.08268	0.00110	0.02562	0.00034	511.2	6.6

MS. The ICP-MS settings were the following: ICP RF Power at 1550 W, cooling gas (Ar) at 15 l/min, auxiliary gas (Ar) at 0.96 l/min and a dual detector mode was used. For each analysis, acquisition time was 30 s for background, 30 s for external standard (NIST 610) and between 15 to 30 s (75 to 150 laser pulses) for rutile mineral analysis depending on the size and thickness of each crystal. External standard used was NIST 610 silicate glass (Pearce et al., 1997 for concentrations), and ^{47}Ti was used as internal standard. Identified minerals were imaged and analyzed before LA-ICP-MS analyzes using a SEM (Hitachi S-4800) and an electron microprobe (Cameca computer-controlled SX-100, GeoRessources, Nancy, France) respectively. TiO_2 content was assumed to be 100 wt%. Silicate glass NIST612 and rutile R10 (Luvizotto et al., 2009) were used as cross-calibration samples and to certify the accuracy and precision of the measurements on the unknown rutiles. Acquisition times were: 0.01 s for ^{47}Ti, 0.02 s for ^{53}Cr and ^{93}Nb, and 0.05 s for ^{90}Zr and ^{91}Zr. Total cycle time was 367 ms. Data were treated with the "Iolite" software (Paton et al., 2011). Zr-in-rutile temperatures were calculated using the thermometer defined by Zack et al. (2004a):

$$T\,(\text{in }^{\circ}C) = 127.8 \times \ln(Zr \text{ in ppm}) - 10.$$

The uncertainty on the computation of temperatures using this thermometer is of ±50 °C and is inherited from the temperature estimations of the natural samples used to calibrate this thermometer (Zack et al., 2004a). The concentration of Zr in rutile grains should be buffered by coexisting zircon and quartz phases (Zack et al., 2004a).

5. Petrographic and microstructural description of the micaschists

5.1. Lithologies

The Lumwana micaschists typically comprise garnet-micaschists layers alternating with kyanite-micaschists at the scale of tens of centimeters (Fig. 5). The so-called "ore schists", correspond to the sulfide-rich kyanite-micaschists (pyrrhotite, chalcopyrite and bornite) whereas the garnet-micaschists, kyanite-free, contain very little sulfides.

5.2. Metamorphic fabrics

The kyanite- and garnet-micaschists show (i) the same grano-lepidoblastic texture and (ii) a superposition of structures associated with distinct mineral paragenesis attributed to three successive deformation stages, D_1, D_2, and D_3 (Figs. 5, 6, 7 and 8).

5.2.1. D_1 deformation-metamorphic stage

The D_1 deformation and metamorphic stage is identified by the preservation of an $S_{0/1}$ foliation as relics in microlithons or as inclusions in some porphyroblasts. This foliation is delineated by (i) fine-grained layers of quartz (Qz_1, Fig. 8a), plagioclase, rutile, alternating with mica-rich layers, (ii) rounded zircons and altered Co–Fe–Ni sulfides grains (Fig. 9a), (iii) quartz veins (Qz_2) transposed into the later S_2 schistosity (Figs. 6 and 7) and locally containing pyrrhotite and (iv) a first generation of rounded kyanite poikiloblasts (Ky_1, Fig. 8b) crystallized during late-D_1 deformation and containing oriented inclusions of

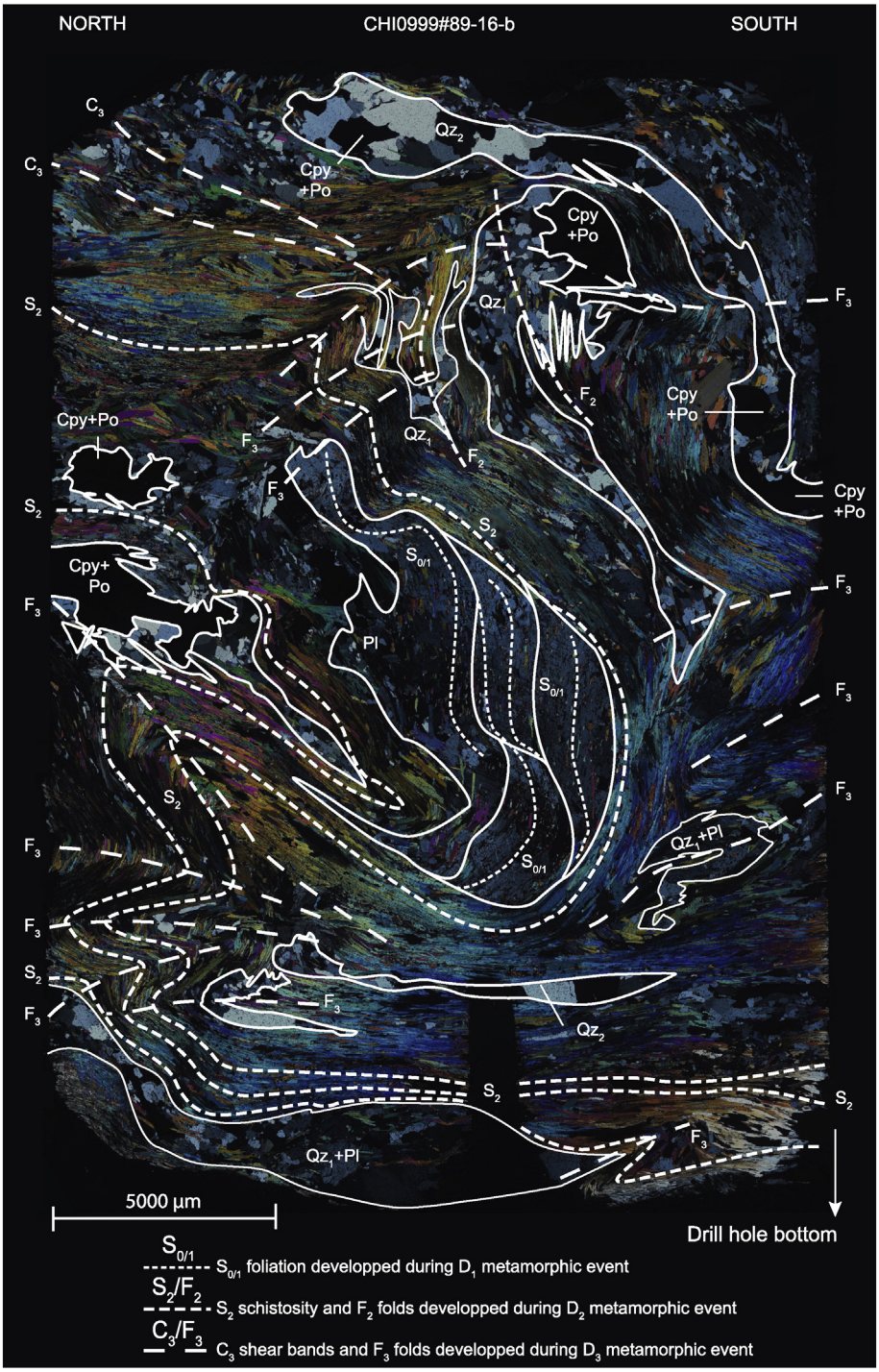

Fig. 6. Photograph of sample CHI0999#89-16-b under microscope (polarized and analyzed light) interpreted by adding the three metamorphic event microstructures. Abbreviations: Cpy = chalcopyrite; Pl = plagioclase; Po = pyrrhotite; Qz_1 = first generation of quartz; Qz_2 = second generation of quartz.

graphite, rutile, bornite, chalcopyrite and digenite (Fig. 9b). These same oriented inclusions delineate the $S_{0/1}$ foliation in late-D_1 porphyroblasts of plagioclase (Figs. 6 and 8c).

5.2.2. D_2 deformation-metamorphic stage

A steep-dipping S_2 schistosity wraps late-D_1 plagioclase porphyroblasts (Fig. 8c), transposes D_1 metamorphic fabrics (Fig. 8a) and is expressed by the preferred orientation of the phlogopite and muscovite (001) cleavage planes. This S_2 schistosity is preserved in the least deformed zones of the kyanite-micaschists (e.g. sample CHI0999#89-16-b, Fig. 6) and is transposed in the later S_3 schistosity (e.g. sample CHI0999#93-17-a, Fig. 10a).

5.2.3. D_3 deformation-metamorphic stage

The main metamorphic fabric developed in Lumwana's kyanite-micaschists is a shallow-dipping S_3 schistosity which is associated with top to the south kinematic criteria. This schistosity is delineated by the preferred orientation of the phlogopite and muscovite (001) cleavage planes alternating with quartz-rich layers (Fig. 7), forming the grano-lepidoblastic texture of the micaschists. This D_3 metamorphic event transposes previous fabrics and quartz veins (Qz_1 and Qz_2, Fig. 7).

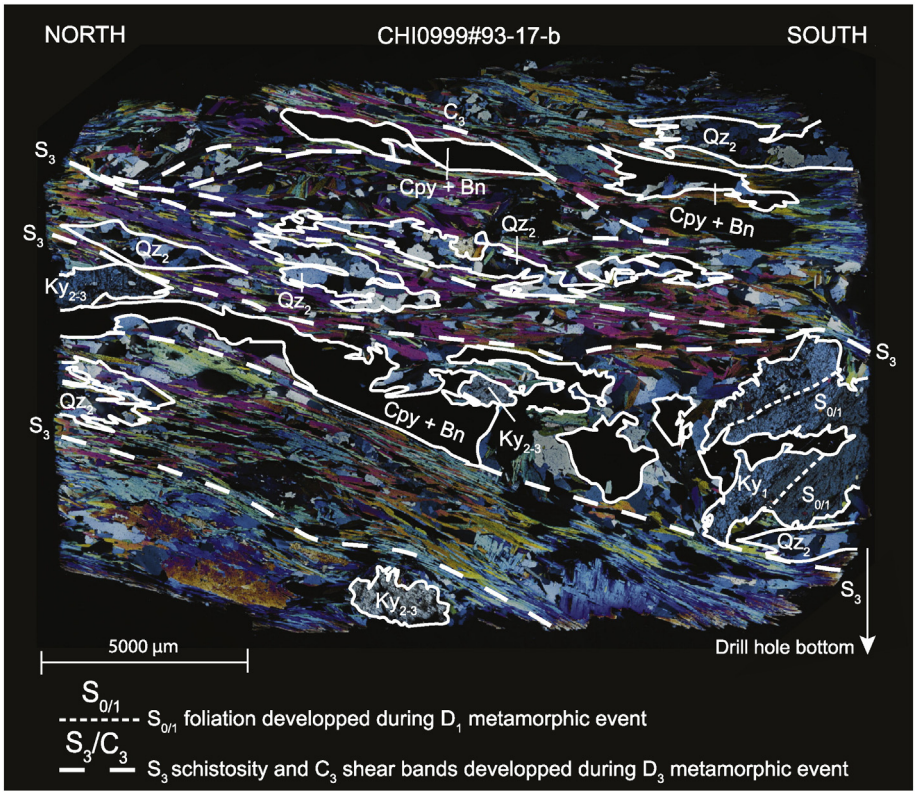

Fig. 7. Photograph of sample CHI0999#93-17-b under microscope (polarized and analyzed light) interpreted by adding the metamorphic event microstructures. Abbreviations: Bn = bornite; Cpy = chalcopyrite; Ky_1 = first generation of kyanite; Ky_{2-3} = second generation of kyanite transposed in the S_3 schistosity; Qz_1 = first generation of quartz; Qz_2 = second generation of quartz.

It is in an axial planar position of F_3 chevron and isoclinal folds affecting the S_2 schistosity (sample CHI0999#89-16-b, Fig. 6). Phlogopite and muscovite wrap Ky_1 grains, and are parallel to the preferred orientation of a second generation of syn-kinematic kyanite porphyroblasts (Ky_2, Fig. 8d) kinked and wrapped into the S_3 schistosity. These features evidence their crystallization during the D_2 metamorphic stage and their transposition/recrystallization into the D_3 metamorphic fabric (Ky_{2-3}, Fig. 8d). These Ky_{2-3} porphyroblasts are associated with chalcopyrite, bornite, monazite and rutile which delineate this fabric. The D_3 deformation stage is ended by shallow-dipping top to the north C_3 shear zones (Figs. 5, 6 and 7) cross-cutting the S_3 schistosity (Fig. 7).

5.3. Petrography of the major metamorphic phases in micaschists

Muscovite and phlogopite define the matrix of the micaschists. Black micas grains are phlogopite with a mean X_{Mg} value equal to 0.851 and 0.633 for pre-D_3 and syn-D_3 grains respectively (Table 2). There are two types of quartz veins transposed in the S_3 foliation (Figs. 6, 7 and 8a). Qz_1 veins are dominated by quartz grains with a heterogeneous size but not exceeding a few micrometers in diameter, but also contain plagioclase and micas. Qz_2 veins are dominated by quartz grains with a much larger diameter (10 to several tens of micrometers wide), also contain plagioclase but no micas. They often contain sulfides such as chalcopyrite–pyrrhotite or bornite–chalcopyrite (Figs. 6 and 7). Plagioclase grains from the matrix may contain elongated inclusions of micas and/or graphite defining an inherited $S_{0/1}$ foliation (Fig. 8c). Late-D_3 shear bands are associated with (i) the retrogression of phlogopite into chlorite (Fig. 8f), (ii) crystallization of tourmaline, rutile and pyrite and (iii) transposition of sulfides.

Alternating with these Cu-rich kyanite-micaschists, barren garnet-micaschists display the same textures and a similar mineralogy to the exception of the absence of kyanite and sulfides and the presence of garnet poikiloblasts with no pressure shadow. These poikiloblasts contain oriented inclusions of phlogopite, chlorite, plagioclase, quartz and rutile, mostly parallel to the S_3 schistosity. According to these textural features, garnet poikiloblasts are interpreted as being coeval with the development of the S_3 schistosity, i.e. are syn-D_3 metamorphic stage. However, in a few of these poikiloblasts the oriented inclusions display a slight rotation compared to the orientation of the surrounding S_3 schistosity, leading to propose that these poikiloblasts partially grew during D_2 event before being transposed/recrystallized during the development of the S_3 schistosity and are thus denominated as syn-D_{2-3} garnet poikiloblasts.

5.4. Textural position of Cu-bearing ore minerals and of accessory minerals

5.4.1. Sulfides

Cu mineralization is only present in the kyanite-micaschists, i.e. Cu sulfides do not coexist with garnet. Cu is expressed as two sulfide assemblages that are spatially disconnected, namely (i) chalcopyrite–pyrrhotite and (ii) chalcopyrite–bornite. Pyrrhotite is only present in the upper part of the micaschists and is absent in sample CHI0999#93-17. Bornite is only present in the lower part of the drill-core, in sample CHI0999#93-17 at the base of a kyanite-micaschists layer and is typically intergrown with chalcopyrite (Fig. 9c).

The first generation of sulfides predates the D_1 phase as indicated by a bornite-rich/chalcopyrite-poor assemblage (in the lower part of the drill-hole), locally associated with a few digenite grains, enclosed into Ky_1 (Fig. 9b), and chalcopyrite enclosed into late-D_1 porphyroblasts of plagioclase. Bornite and chalcopyrite may also be enclosed into Ky_2. In addition to this paragenesis, chalcopyrite and pyrrhotite/bornite are also present in quartz veins (Qz_2) that are transposed into the S_2 and in the S_3 schistosities.

The second generation of sulfides is associated with the development of the D_2 metamorphic fabrics (steep-dipping S_2 schistosity) as a

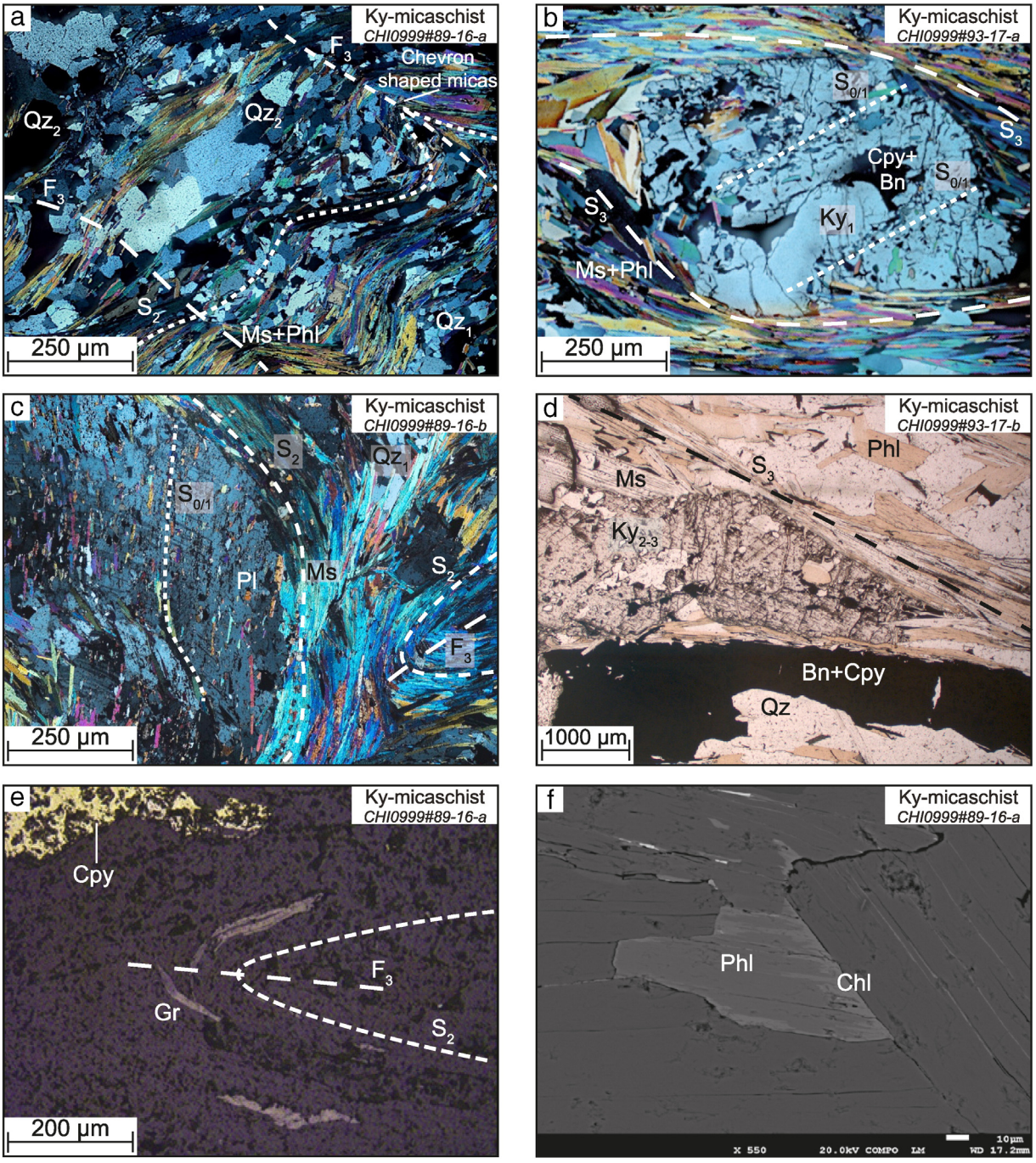

Fig. 8. Photomicrographs illustrating kyanite-micaschists petrography and microstructures from samples CHI0999#89-16-a, -16-b, #93-17-a and #93-17-b. a: first (Qz_1) and second (Qz_2) generations of quartz. Second generation veins are transposed in the S_2 schistosity, delineated by muscovite and phlogopite cleavage plane alignment. The whole paragenesis is deformed by the later D_3 metamorphic event (polarized and analyzed light); b: first generation of kyanite with enclosed chalcopyrite, bornite and $S_{0/1}$ foliation. Kyanite's sigmoidal shape is made by the S_3 schistosity, indicating that Ky_1 crystallized before this event (polarized and analyzed light); c: $S_{0/1}$ foliation enclosed in porphyroblasts of plagioclase which are wrapped by the S_2 schistosity, delineated by muscovite and veins of first generation of quartz (Qz_1) (polarized and analyzed light); d: second generation of kyanite porphyroblasts transposed in the S_3 schistosity (polarized unanalyzed light); e: graphite associated with the S_2 schistosity and deformed by the S_3 schistosity indicating that carbon was introduced before both metamorphic events (reflected light); f: phlogopite grain altered by chloritisation (SEM). Abbreviations: Bn = bornite; Chl = chlorite; Cpy = chalcopyrite; Gr = graphite; Ky_1 = first generation of kyanite; Ky_{2-3} = second generation of kyanite transposed in the S_3 schistosity; Ms = muscovite; Phl = phlogopite; Pl = plagioclase; Qz_1 = first generation of quartz; Qz_2 = second generation of quartz.

chalcopyrite–pyrrhotite assemblage (sample CHI0999#89-16-b) and a chalcopyrite–bornite assemblage (sample CHI0999#93-17-a) in the matrix of the micaschists, parallel with S_2 delineated by phlogopite and muscovite (001) cleavage planes.

The third generation of sulfides, and the best expressed, is associated with the development of the D_3 metamorphic fabrics (S_3 schistosity). A bornite-poor/chalcopyrite-rich assemblage is expressed in pressure shadows of Ky_1 in association with micas delineating the S_3 schistosity wrapped around Ky_1 porphyroclasts (Figs. 7 and 8b). The same sulfides assemblage delineates the S_3 schistosity and is elongated parallel to the (001) cleavage plane of micas (Fig. 8d). Chalcopyrite and bornite are also cogenetic with Ky_{2-3} porphyroblasts (Fig. 8d).

Finally, the sulfides are locally transposed into C_3 shear bands indicating that they were remobilized and recrystallized during late-D_3.

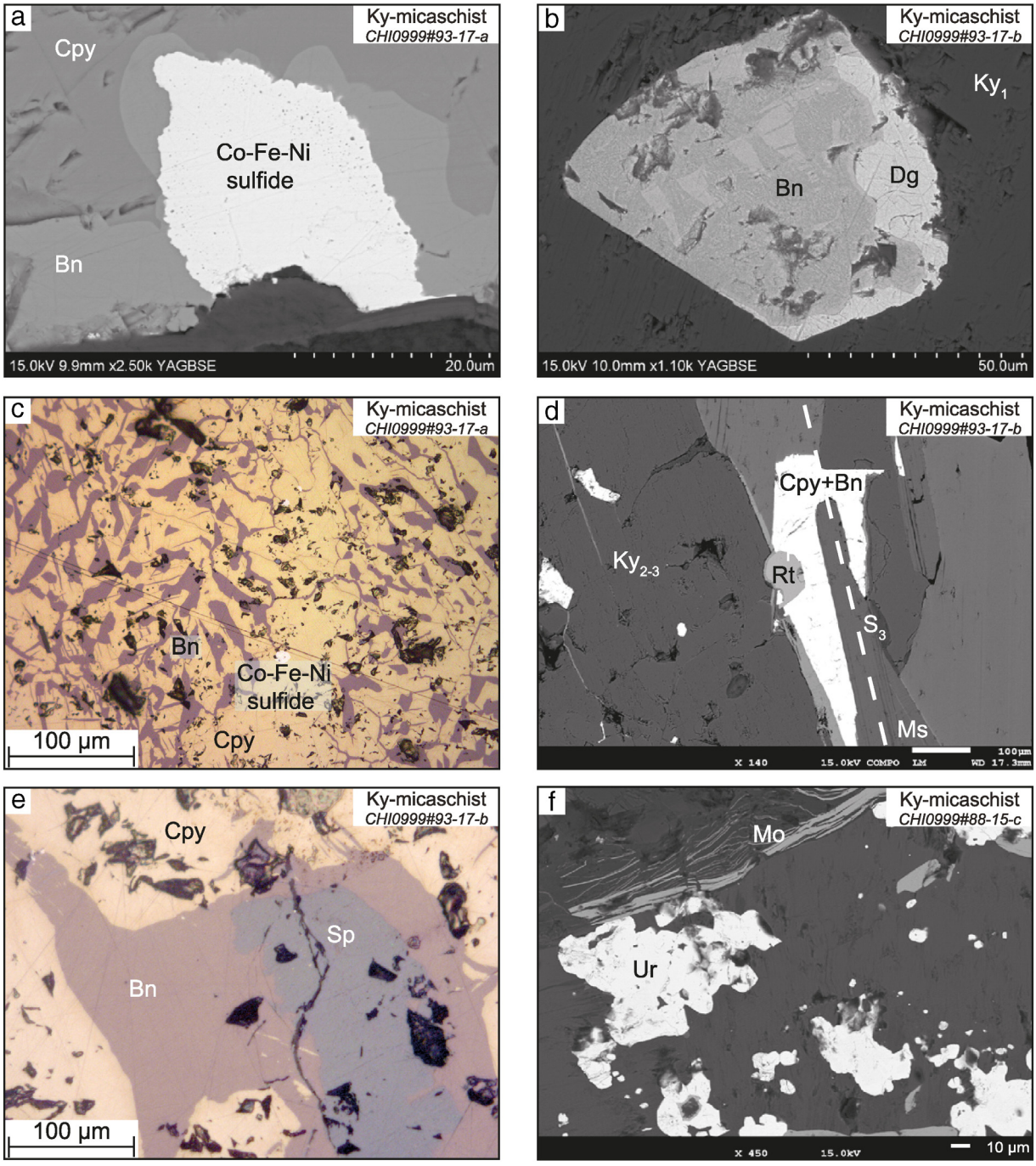

Fig. 9. Photomicrographs illustrating the mineralization of kyanite-micaschists from samples CHI0999#88-15-c, #93-17-a and 17-b. a: altered Co–Fe–Ni sulfides grain. This mineral is enclosed into syn-S_3 bornite and chalcopyrite (SEM); b: digenite grain surrounding a bornite crystal. Both are enclosed into Ky_1 (SEM); c: syn-S_3 bornite and chalcopyrite intergrowth features including a few Co–Fe–Ni sulfides grains (reflected light); d: relation between second generation of kyanite (Ky_{2-3}), Cu-rich phases (chalcopyrite and bornite) and rutile. Ky_{2-3}, mineralization, rutile and S_3 are synchronous (SEM); e: sphalerite grain enclosed into bornite. Bornite and chalcopyrite are synchronous with the S_3 schistosity (reflected light); f: relationships between uraninite and molybdenite (SEM). Abbreviations: Bn = bornite; Cpy = chalcopyrite; Dg = digenite; Ky_1 = first generation of kyanite; Ky_{2-3} = second generation of kyanite transposed in the S_3 schistosity; Mo = molybdenite; Ms = muscovite; Po = pyrrhotite; Rt = rutile; Sp = sphalerite; Ur = uraninite.

5.4.2. Monazite

Monazite grains are present in various textural positions, namely (i) delineating the S_2 schistosity in axial planar position of F_3 folds (Fig. 10a), (ii) within the S_3 schistosity (Fig. 10b), (iii) as inclusion in syn-S_3 Cu sulfides (Fig. 10c), and (iv) intergrown with syn-S_3 Cu sulfides (Fig. 10d). It is interesting to note that these monazite grains are not wrapped by micas delineating the S_3 schistosity but intergrown with them, and that these grains do not show any signs of a detrital origin (rounded shape or percussion marks).

Monazite grains associated with relics of the S_2 schistosity affected by F_3 folds are interpreted as having crystallized during the D_2 metamorphic event and as being partially transposed/recrystallized into the D_3 metamorphic fabrics. Chemical compositions of the representative monazite are reported in Table 3 and indicate that the P_2O_5 content of the analyzed grains is quite homogeneous (29.12 to 31.07 wt.%). Even though the studied grains are mostly composed of monazite-(Ce) (Ce_2O_3 content from 26.27 to 32.83 wt.%), they display some chemical variations with a correlation between the CaO (0.43 wt.% to 1.65 wt.%)

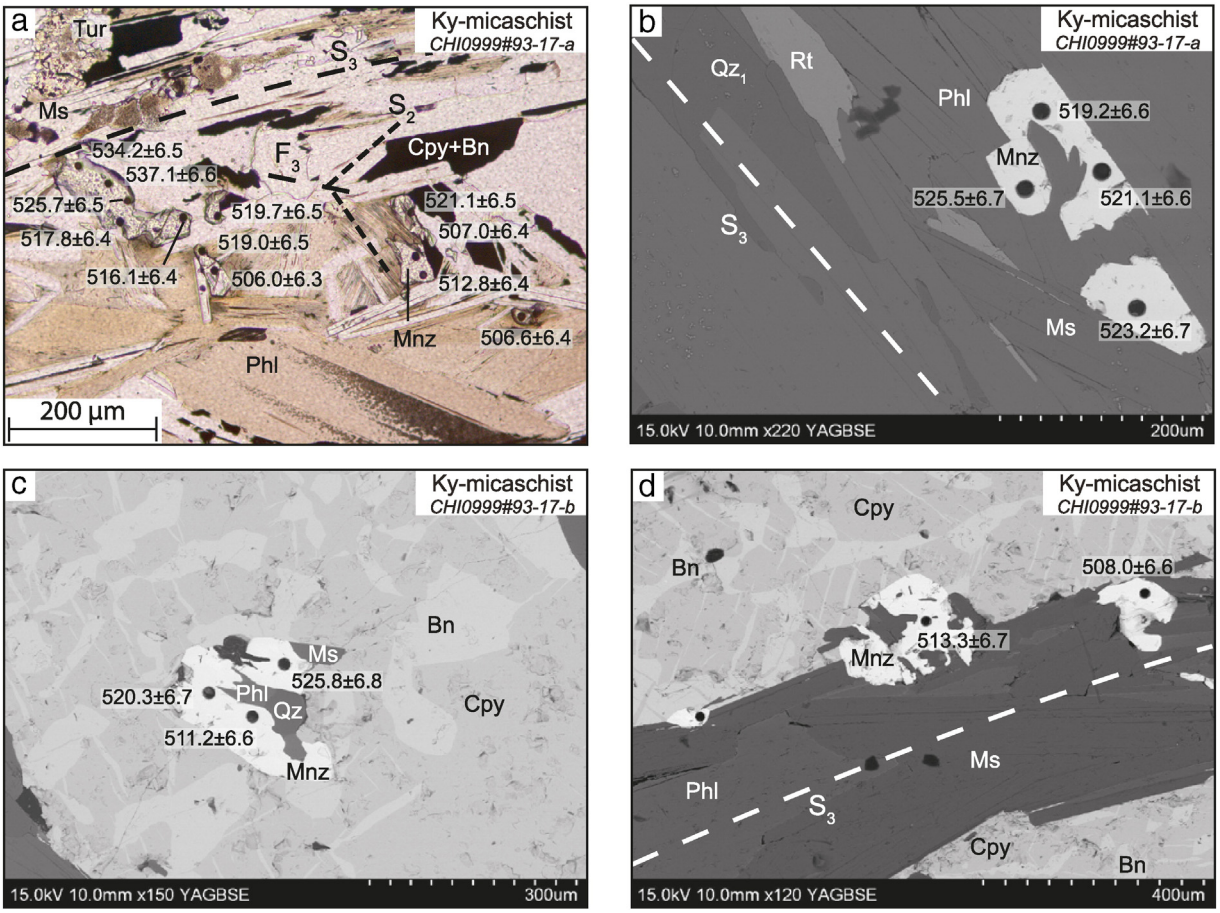

Fig. 10. Photomicrographs illustrating the structural position of monazite grains, their relationship with mineralization and matrix from samples CHI0999#93-17-a and 17-b, the position of ablation spots made during U–Th–Pb dating and ages of each of these spots. a: monazite grains synchronous with Cu sulfides and their relation with the S_2 (folded by F_3 isoclinal folds) and S_3 schistosities (polarized unanalyzed light); b: monazite grains synchronous with the development of the S_3 schistosity (SEM); c: monazite crystal enclosed into syn-S_3 Cu sulfides (SEM); d: monazite grains synchronous with Cu sulfides and with the S_3 schistosity (SEM). Abbreviations: Bn = bornite; Cpy = chalcopyrite; Gr = graphite; Mnz = monazite; Ms = muscovite; Phl = phlogopite; Qz = quartz; Qz_1 = first generation of quartz; Rt = rutile; Tur = tourmaline.

and ThO_2 (2.04 wt.% to 10.60 wt.%) contents. Similarly, the Ce_2O_3 content is correlated with La_2O_3 (10.18 wt.% to 13.20 wt.%). These variations of REE^{3+} are negatively correlated with the CaO and ThO content variations. This is consistent with the brabantite substitution (Rose, 1980), involving the reaction described by Poitrasson et al. (2000): $2REE^{3+} \Leftrightarrow Th^{4+} + Ca^{2+}$ (Fig. 13a; Spear and Pyle, 2002).

5.4.3. Rutile

Rutile grains are present in all metamorphic paragenesis, namely (i) as inclusions in Ky_1 predating the D_1 deformation-metamorphic stage; (ii) coeval with garnet poikiloblasts (Fig. 11a); (iii) aligned along the (001) cleavage plane of micas delineating the S_3 schistosity and thus synchronous with the syn-D_3 Cu sulfides and Ky_{2-3} porphyroblasts (Figs. 9d, 11b and c) and (iv) associated with sulfides in shear bands developed during late-D_3 metamorphic stage (Fig. 11d). However, pre-D_1 grains were not large enough to conduct LA-ICP-MS analyzes.

Rutile grains from garnet-micaschists (sample CHI0999#88-13) are chemically different than the ones from the kyanite-micaschists (Table 4) with (i) Cr from 329 to 526 ppm in the kyanite-micaschists and from 65 to 84 ppm in the garnet-micaschists, (ii) ^{90}Zr from 76 to 140 ppm in the kyanite-micaschists and from 59 to 74 ppm in the garnet-micaschists, (iii) ^{91}Zr from 77 to 142 ppm in the kyanite-micaschists and from 59 to 73 ppm in the garnet-micaschists and (iv) Nb from 3390 to 7300 ppm in the kyanite-micaschists and from 2400 to 5650 ppm in the garnet-micaschists. Results obtained for the Cr and Nb contents have been plotted in a Cr vs Nb diagram (Fig. 14a).

5.4.4. Other accessory minerals

Zircon grains are a few micrometers wide and are enclosed into the quartz–plagioclase matrix and/or into micas delineating the $S_{0/1}$ foliation and the S_2 and S_3 schistosities. Graphite flakes delineate S_2 (Fig. 8e) and S_3 schistosities and are present as inclusions in both generation of kyanite (Ky_1 and Ky_{2-3}) porphyroblasts. A few apatite grains are in textural equilibrium with the syn-D_2 chalcopyrite–pyrrhotite assemblage. Retrograde chlorite (partial alteration of phlogopite, Fig. 8f) is also present in garnet poikiloblasts.

In addition to the main sulfide assemblages, a few grains of Co–Fe–Ni sulfides are also present and show rounded shapes and evidence of alteration (Fig. 9a and c). Similarly, a few sphalerite grains are present as inclusions in the Cu sulfides (Fig. 9e). Uranium is expressed in the kyanite-micaschists as uraninite grains which, according to their microstructural position and shape, pre-date small euhedral pyrite grains. Uraninite may also be associated with molybdenite which delineates the S_3 schistosity (Fig. 9f).

According to these microstructural and petrographic observations, the three different deformations and metamorphic stages are summarized in the paragenetic sequence proposed in Fig. 12.

6. Geochronological and thermometric constraints

In this section, we provide new geochronological and thermometric constraints for the metamorphic deformation stages that have been defined in the previous sections.

Table 2
Average mineral compositions with confidence interval of 95% in brackets (n = number of samples) from samples CHI0999#88-13, 89-16-b and 93-17-b. Abbreviations: Chl = chlorite; Ms = muscovite; Phl = phlogopite.

Mineral		Phl		Chl		Ms	
Structural position		Pre-D_3	Syn-D_3	Pre-D_3	Late-D_3	Syn-D_2	Syn-D_3
Sample		93-17-b	89-16-b	88-13	89-16-b	89-16-b	89-16-b
Oxides wt.%	SiO_2	39.65	36.73	24.25	27.67	46.65	46.44
		(0.34)	(0.35)	(0.37)	(2.25)	(0.40)	(0.41)
	TiO_2	1.04	1.40	0.04	0.21	0.74	0.70
		(0.06)	(0.07)	(0.02)	(0.28)	(0.04)	(0.08)
	Al_2O_3	18.24	18.70	22.17	18.24	33.80	33.96
		(0.19)	(0.16)	(0.24)	(0.48)	(0.52)	(0.53)
	FeO	6.16	13.95	26.66	27.80	0.66	0.69
		(0.23)	(0.85)	(1.33)	(3.79)	(0.09)	(0.06)
	MnO	0.03	0.05	0.07	0.05	0.01	0.03
		(0.01)	(0.02)	(0.03)	(0.04)	(0.01)	(0.01)
	MgO	19.76	13.65	12.81	12.09	1.45	1.33
		(0.25)	(0.84)	(1.13)	(1.20)	(0.15)	(0.21)
	CaO	0.03	0.07	0.05	0.11	0.02	0.05
		(0.02)	(0.08)	(0.02)	(0.06)	(0.01)	(0.02)
	Na_2O	0.42	0.26	0.03	0.06	0.89	0.85
		(0.03)	(0.09)	(0.02)	(0.06)	(0.06)	(0.04)
	K_2O	9.12	9.61	0.06	1.06	9.86	9.88
		(0.13)	(0.19)	(0.07)	(1.87)	(0.17)	(0.14)
	Total	98.69	98.49	88.18	87.33	98.59	98.38
		(0.22)	(0.30)	(0.32)	(1.74)	(0.66)	(0.58)
Oxygens		22	22	14	14	11	11
Cations	Si	5.662	5.489	2.499	1.057	6.255	6.254
		(0.035)	(0.027)	(0.280)	(0.343)	(0.031)	(0.040)
	Al^{IV}	2.338	2.511	1.644	0.515	1.745	1.746
		(0.035)	(0.027)	(0.207)	(0.197)	(0.031)	(0.040)
	Al^{VI}	0.733	0.785	1.056	0.327	3.595	3.645
		(0.028)	(0.023)	(0.123)	(0.108)	(0.034)	(0.066)
	Ti	0.111	0.157	0.003	0.004	0.075	0.071
		(0.006)	(0.009)	(0.001)	(0.004)	(0.004)	(0.008)
	Fe^{tot}	0.736	1.747	2.327	0.937	0.075	0.070
		(0.028)	(0.115)	(0.383)	(0.363)	(0.010)	(0.018)
	Mn	0.003	0.006	0.007	0.001	0.001	0.003
		(0.002)	(0.003)	(0.004)	(0.001)	(0.001)	(0.002)
	Mg	4.207	3.035	1.936	0.687	0.289	0.254
		(0.052)	(0.169)	(0.137)	(0.221)	(0.030)	(0.052)
	Ca	0.005	0.012	0.006	0.005	0.003	0.003
		(0.002)	(0.013)	(0.004)	(0.004)	(0.057)	(0.002)
	Na	0.117	0.077	0.005	0.004	0.230	0.227
		(0.009)	(0.027)	(0.005)	(0.002)	(0.016)	(0.017)
	K	1.661	1.833	0.008	0.029	1.687	1.483
		(0.024)	(0.039)	(0.010)	(0.046)	(0.038)	(0.388)
	X_{Mg}	0.851	0.633	0.460	0.442	–	–
		(0.06)	(0.028)	(0.038)	(0.066)		
	n	16	19	8	10	16	8

6.1. U–Th–Pb dating on syn- to late-metamorphic monazite

In monazite, ^{206}Pb and ^{208}Pb are the most abundant Pb isotopes. In addition, monazite grains from Lumwana's micaschists present a non-negligible substitution to brabantite (Fig. 13a, Poitrasson et al., 2000; Rose, 1980), increasing the abundance of Th and thus relatively decreasing the U one. Accordingly, the $^{235}U/^{207}Pb$ chronometer is associated with a large uncertainty, it is therefore more pertinent to look at the data in a $^{206}Pb/^{238}U$ versus $^{208}Pb/^{232}Th$ Concordia diagram. Twelve monazite grains from sample CHI0999#93-17-a and six from sample CHI0999#93-17-b have been analyzed (Table 1).

Plotted in a $^{206}Pb/^{238}U$ vs $^{208}Pb/^{232}Th$ Concordia diagram (Fig. 13b), data from sample CHI0999#93-17-a and -b are concordant to sub-concordant and spread along the Concordia curve. These monazite grains are related to D_2 deformation-metamorphic stage and transposed and partially recrystallized during D_3 deformation-metamorphic stage. Their recrystallization is thus synchronous with the syn-D_3 Cu mineralization and/or with the development of the S_3 schistosity. These syn-D_{2-3} monazite grains display apparent $^{208}Pb/^{232}Th$ dates ranging from 537.1 ± 6.6 to 502.8 ± 6.3 Ma (Table 1). The scattering in the ages (Fig. 13c) tends to show differences between the different crystals and is interpreted to record a continuum of crystallization from ca. 540 Ma down to ca. 500 Ma.

6.2. Thermometric constraints on the metamorphic path

Even though three generations of rutile are represented in our samples, pre-D_1 grains were not large enough to conduct Zr-in-rutile thermometry analyzes. Two populations of rutile grains have thus been investigated in order to constrain the temperature reached during these metamorphic stages: (i) rutile grains delineating the S_3 schistosity (parallel to muscovite and phlogopite (001) cleavage planes) and (ii) rutile grains associated with late-D_3 shear bands, using the Zack et al. (2004a) thermometer which is based on the concentration of Zr in rutile. In addition, as the temperature depends on the concentration of Zr in the matrix (Zack et al., 2004a), we choose to limit our temperature computations to rocks with a similar mineralogy and thus an identical chemical composition, i.e. only in kyanite-micaschists where zircon and quartz are coexisting phases and not in garnet-micaschists in which no zircon grains are observed associated with rutile grains.

Table 3
Representative monazite analyses from samples CHI0999#93-17-a & -17-b obtained using EMP.

Sample		93-17-a	93-17-a	93-17-a	93-17-a	93-17-a	93-17-a	93-17-a	93-17-a	93-17-a	93-17-a	93-17-a	93-17-a	93-17-a	93-17-a	93-17-a	93-17-a	93-17-a	93-17-a
Analysis no.		1-1	1-2	1-3	1-4	1-5	1-6	1-7	1-9	1-10	1-11	1-12	1-13	1-14	2-1	2-2	2-3	2-4	2-5
Oxides/wt.%	P_2O_5	30.17	30.35	30.01	30.62	30.18	30.49	30.31	29.81	29.93	30.17	30.58	30.06	30.02	30.00	30.15	30.02	30.66	30.32
	SiO_2	0.38	0.32	0.37	0.34	0.32	0.55	0.29	0.46	0.49	0.32	0.37	0.33	0.39	0.42	0.39	0.35	0.44	0.32
	CaO	0.80	0.62	0.72	0.67	0.65	1.07	0.53	0.84	1.07	0.61	0.76	0.68	0.78	1.17	0.82	0.69	0.94	0.69
	Y_2O_3	1.96	1.83	1.95	1.93	1.96	2.44	1.87	1.98	2.49	1.84	2.00	1.75	1.84	2.41	2.25	1.75	2.40	1.67
	La_2O_3	12.32	12.58	12.29	12.51	12.50	11.52	12.49	12.44	11.47	12.66	12.28	12.78	12.85	11.78	12.00	12.53	11.76	13.09
	Ce_2O_3	30.92	31.75	31.22	31.65	31.59	29.28	32.06	30.98	29.34	31.57	31.21	31.72	31.72	29.57	30.37	31.24	29.88	31.86
	Pr_2O_3	3.39	3.41	3.27	3.54	3.43	3.21	3.56	3.25	3.17	3.49	3.34	3.53	3.34	3.33	3.35	3.32	3.34	3.50
	Nd_2O_3	12.09	12.23	12.41	12.33	12.37	11.63	12.50	11.81	11.70	12.15	12.06	12.13	12.02	11.49	11.98	12.17	12.01	11.95
	Sm_2O_3	1.97	1.99	2.05	1.99	2.08	1.86	2.10	2.00	2.06	2.06	1.97	1.93	1.81	1.99	1.99	2.11	2.11	2.00
	Gd_2O_3	1.37	1.41	1.32	1.31	1.44	1.48	1.32	1.30	1.51	1.49	1.43	1.30	1.34	1.44	1.49	1.46	1.53	1.34
	PbO	0.14	0.12	0.15	0.13	0.12	0.20	0.09	0.14	0.20	0.11	0.13	0.11	0.13	0.21	0.17	0.13	0.17	0.10
	ThO_2	3.85	3.20	3.66	3.37	3.25	6.05	2.55	4.33	5.94	2.84	4.02	3.49	4.11	5.55	4.33	3.65	4.97	3.10
	UO_2	0.51	0.40	0.44	0.43	0.44	0.65	0.38	0.42	0.66	0.40	0.44	0.42	0.51	0.79	0.64	0.45	0.65	0.40
	Total	99.87	100.22	99.86	100.84	100.31	100.44	100.04	99.77	100.02	99.70	100.59	100.22	100.85	100.16	99.93	99.88	100.86	100.33
Oxygens		4	4	4	4	4	4	4	4	4	4	4	4	4	4	4	4	4	4
Cations	P	0.993	0.996	0.991	0.997	0.992	0.993	0.996	0.986	0.986	0.995	0.997	0.990	0.986	0.987	0.992	0.992	0.995	0.994
	Si	0.015	0.012	0.014	0.013	0.012	0.021	0.011	0.018	0.019	0.012	0.014	0.013	0.015	0.016	0.015	0.014	0.017	0.012
	ΣT-site	1.008	1.008	1.005	1.010	1.004	1.014	1.007	1.004	1.005	1.007	1.011	1.003	1.001	1.003	1.007	1.005	1.012	1.007
	Ca	0.033	0.026	0.030	0.028	0.027	0.044	0.022	0.035	0.045	0.025	0.031	0.028	0.032	0.049	0.034	0.029	0.039	0.029
	Y	0.041	0.038	0.040	0.039	0.040	0.050	0.039	0.041	0.052	0.038	0.041	0.036	0.038	0.050	0.047	0.036	0.049	0.034
	La	0.177	0.180	0.177	0.177	0.179	0.163	0.179	0.179	0.165	0.182	0.174	0.183	0.184	0.169	0.172	0.180	0.166	0.187
	Ce	0.440	0.451	0.446	0.446	0.449	0.412	0.456	0.443	0.418	0.450	0.440	0.452	0.450	0.421	0.432	0.446	0.419	0.452
	Pr	0.048	0.048	0.046	0.050	0.049	0.045	0.050	0.046	0.045	0.050	0.047	0.050	0.047	0.047	0.047	0.047	0.047	0.049
	Nd	0.168	0.169	0.173	0.169	0.171	0.160	0.173	0.165	0.163	0.169	0.166	0.169	0.166	0.159	0.166	0.170	0.164	0.165
	Sm	0.026	0.027	0.028	0.026	0.028	0.025	0.028	0.027	0.028	0.028	0.026	0.026	0.024	0.027	0.027	0.028	0.028	0.027
	Gd	0.018	0.018	0.017	0.017	0.019	0.019	0.017	0.017	0.019	0.019	0.018	0.017	0.017	0.019	0.019	0.019	0.019	0.017
	Pb	0.001	0.001	0.002	0.001	0.001	0.002	0.001	0.001	0.002	0.001	0.001	0.001	0.001	0.002	0.002	0.001	0.002	0.001
	Th	0.034	0.028	0.032	0.029	0.029	0.053	0.023	0.039	0.053	0.025	0.035	0.031	0.036	0.049	0.038	0.032	0.043	0.027
	U	0.004	0.003	0.004	0.004	0.004	0.006	0.003	0.004	0.006	0.003	0.004	0.004	0.004	0.007	0.006	0.004	0.006	0.003
	Σa-site	0.991	0.989	0.995	0.987	0.996	0.979	0.991	0.997	0.994	0.991	0.984	0.997	1.002	0.998	0.990	0.994	0.983	0.992
	% Hutt	1.46	1.24	1.43	1.30	1.23	2.12	1.12	1.77	1.88	1.24	1.43	1.27	1.48	1.60	1.50	1.35	1.68	1.23
	% Brab	7.76	6.07	7.01	6.51	6.35	10.36	5.22	7.92	10.35	5.97	7.30	6.55	7.49	11.29	8.22	6.76	9.17	6.56
	% Mnz	90.78	92.70	91.57	92.19	92.43	87.52	93.66	90.31	87.76	92.80	91.28	92.18	91.02	87.12	90.27	91.88	89.15	92.22

Sample		93-17-a	93-17-a	93-17-a	93-17-a	93-17-a	93-17-a	93-17-a	93-17-a	93-17-a	93-17-a	93-17-a	93-17-a	93-17-a	93-17-a	93-17-a	93-17-a	93-17-a	93-17-a
Analysis no.		2-6	2-7	2-8	2-9	2-10	3-1	3-2	4-1	4-2	4-3	4-4	8-1	8-2	9-1	9-2	9-4	9-5	9-6
Oxides/wt.%	P_2O_5	31.07	30.00	30.21	30.67	30.61	30.41	30.55	30.26	30.53	29.12	30.67	30.19	29.84	30.23	29.70	29.59	29.79	30.40
	SiO_2	0.37	0.46	0.34	0.34	0.31	0.31	0.46	0.40	0.33	1.00	0.31	0.31	0.31	0.37	0.36	0.33	0.37	0.36
	CaO	0.85	0.85	0.77	0.58	0.59	0.55	0.90	0.79	0.64	0.64	0.55	0.61	0.43	0.66	0.68	0.63	0.70	0.84
	Y_2O_3	2.69	1.88	2.37	1.66	1.78	1.68	2.11	1.79	2.04	1.61	1.72	2.04	1.65	1.99	2.13	1.78	1.95	2.26
	La_2O_3	11.86	12.08	12.20	12.54	12.57	12.67	11.89	12.41	12.30	12.21	12.85	12.80	13.20	12.56	12.58	12.86	12.63	12.34
	Ce_2O_3	29.75	30.67	30.44	31.60	31.60	31.92	30.20	30.78	31.01	30.89	31.91	31.77	32.83	31.29	31.39	31.79	31.38	31.13
	Pr_2O_3	3.35	3.43	3.43	3.41	3.41	3.51	3.44	3.37	3.42	3.30	3.49	3.45	3.50	3.38	3.38	3.47	3.45	3.52
	Nd_2O_3	12.20	12.04	12.07	12.26	12.33	12.45	12.09	12.18	12.35	12.07	12.34	12.07	12.18	12.23	12.20	12.30	12.21	12.26
	Sm_2O_3	2.09	2.02	2.09	1.98	2.07	2.12	1.99	1.98	2.19	1.99	2.00	1.99	2.08	2.12	2.05	2.03	2.05	2.08
	Gd_2O_3	1.55	1.29	1.52	1.43	1.33	1.32	1.41	1.31	1.45	1.25	1.27	1.43	1.41	1.47	1.36	1.31	1.45	1.54
	PbO	0.17	0.15	0.15	0.11	0.11	0.10	0.18	0.15	0.13	0.11	0.10	0.13	0.09	0.13	0.13	0.12	0.14	0.14
	ThO_2	4.32	4.76	3.76	3.08	2.96	2.75	5.12	4.01	3.06	2.83	2.67	3.04	2.04	3.52	3.38	3.11	3.62	3.49
	UO_2	0.63	0.42	0.61	0.38	0.42	0.42	0.46	0.49	0.48	0.39	0.38	0.51	0.44	0.52	0.55	0.45	0.47	0.59
	Total	100.90	100.06	99.97	100.06	100.07	100.20	100.81	99.93	99.94	97.41	100.26	100.34	100.00	100.46	99.90	99.76	100.21	100.94

Oxygens		4	4	4	4	4	4	4	4	4	4	4	4	4	4	4	4	4	4
Cations	P	1.002	0.989	0.993	1.003	1.001	0.997	0.994	0.995	1.000	0.979	1.001	0.992	0.988	0.992	0.985	0.984	0.985	0.991
	Si	0.014	0.018	0.013	0.013	0.012	0.012	0.018	0.016	0.013	0.040	0.012	0.012	0.012	0.014	0.014	0.013	0.014	0.014
	ΣT-site	1.016	1.007	1.006	1.016	1.013	1.009	1.012	1.010	1.013	1.019	1.013	1.004	1.000	1.006	0.999	0.997	0.999	1.005
	Ca	0.035	0.035	0.032	0.024	0.024	0.023	0.037	0.033	0.027	0.027	0.023	0.025	0.018	0.027	0.029	0.027	0.029	0.035
	Y	0.055	0.039	0.049	0.034	0.037	0.035	0.043	0.037	0.042	0.034	0.035	0.042	0.034	0.041	0.044	0.037	0.041	0.046
	La	0.167	0.173	0.175	0.179	0.179	0.181	0.169	0.178	0.175	0.179	0.183	0.183	0.190	0.179	0.182	0.186	0.182	0.175
	Ce	0.415	0.437	0.433	0.447	0.447	0.453	0.425	0.438	0.439	0.449	0.451	0.451	0.470	0.444	0.450	0.457	0.449	0.439
	Pr	0.047	0.049	0.049	0.048	0.048	0.050	0.048	0.048	0.048	0.048	0.049	0.049	0.050	0.048	0.048	0.050	0.049	0.049
	Nd	0.166	0.167	0.167	0.169	0.170	0.172	0.166	0.169	0.171	0.171	0.170	0.167	0.170	0.169	0.171	0.173	0.170	0.169
	Sm	0.027	0.027	0.028	0.026	0.028	0.028	0.026	0.026	0.029	0.027	0.027	0.027	0.028	0.028	0.028	0.027	0.028	0.028
	Gd	0.020	0.017	0.020	0.018	0.017	0.017	0.018	0.017	0.019	0.016	0.016	0.018	0.018	0.019	0.018	0.017	0.019	0.020
	Pb	0.002	0.002	0.002	0.001	0.001	0.001	0.002	0.002	0.001	0.001	0.001	0.001	0.001	0.001	0.001	0.001	0.001	0.001
	Th	0.037	0.042	0.033	0.027	0.026	0.024	0.045	0.035	0.027	0.026	0.023	0.027	0.018	0.031	0.030	0.028	0.032	0.031
	U	0.005	0.004	0.005	0.003	0.004	0.004	0.004	0.004	0.004	0.003	0.003	0.004	0.004	0.004	0.005	0.004	0.004	0.005
	Σa-site	0.975	0.992	0.992	0.977	0.981	0.987	0.983	0.986	0.982	0.982	0.981	0.996	1.002	0.993	1.005	1.007	1.004	0.997
	% Hutt	1.42	1.78	1.31	1.32	1.20	1.20	1.77	1.55	1.28	3.86	1.20	1.19	1.19	1.42	1.38	1.27	1.42	1.36
	% Brab	8.41	8.06	7.69	5.73	5.86	5.49	8.58	7.69	6.40	6.20	5.42	6.15	4.47	6.59	6.78	6.20	6.83	8.06
	% Mnz	90.17	90.16	91.00	92.94	92.94	93.32	89.64	90.76	92.32	89.94	93.38	92.66	94.34	91.99	91.85	92.54	91.76	90.59

Sample		93-17-b	93-17-b	93-17-b	93-17-b	93-17-b	93-17-b	93-17-b	93-17-b	93-17-b	93-17-b	93-17-b	93-17-b	93-17-b	93-17-b	93-17-b
Analysis no.		2-1	2-2	2-3	2-4	3-1	3-2	4-1	5-1	5-2	6-1	6-2	6-3	6-4	6-5	6-6
Oxides/wt.%	P_2O_5	29.92	30.25	30.02	29.47	30.04	30.15	30.20	29.12	30.03	29.19	29.70	30.05	30.25	29.70	29.78
	SiO_2	0.52	0.46	0.56	1.57	0.43	0.44	0.55	1.05	0.96	0.95	0.86	0.41	0.47	0.65	0.57
	CaO	1.25	0.97	1.15	0.90	0.82	0.88	1.07	1.42	1.10	1.65	1.45	0.79	0.93	1.24	1.16
	Y_2O_3	2.50	2.01	2.28	1.63	1.83	1.95	1.90	2.06	2.03	2.58	2.40	1.92	2.09	2.05	2.03
	La_2O_3	11.61	12.11	11.55	11.83	12.43	12.00	11.88	10.74	11.67	10.18	10.61	12.17	11.93	11.56	11.69
	Ce_2O_3	29.01	30.30	29.26	30.05	30.74	30.51	30.00	27.66	29.66	26.27	27.62	30.62	30.08	29.05	28.95
	Pr_2O_3	3.24	3.35	3.23	3.32	3.35	3.39	3.36	3.17	3.27	3.13	3.09	3.53	3.30	3.19	3.10
	Nd_2O_3	11.46	11.86	11.71	11.96	12.11	12.14	11.77	11.27	11.67	10.91	11.24	12.19	11.97	11.42	11.54
	Sm_2O_3	2.05	2.08	2.01	2.13	1.92	2.00	2.13	2.05	2.08	1.97	2.06	2.16	2.05	2.05	1.96
	Gd_2O_3	1.52	1.44	1.50	1.55	1.38	1.54	1.34	1.42	1.44	1.82	1.64	1.48	1.55	1.54	1.53
	PbO	0.26	0.19	0.21	0.15	0.16	0.15	0.20	0.25	0.20	0.30	0.29	0.14	0.17	0.21	0.21
	ThO_2	6.82	5.36	6.59	4.39	4.59	4.82	6.02	8.80	6.12	10.60	9.14	4.27	5.11	7.43	6.81
	UO_2	0.79	0.55	0.57	0.42	0.45	0.43	0.48	0.48	0.44	0.57	0.49	0.43	0.49	0.43	0.46
	Total	100.94	100.94	100.65	99.38	100.23	100.39	100.91	99.51	100.67	100.14	100.57	100.14	100.40	100.53	99.79

Oxygens		4	4	4	4	4	4	4	4	4	4	4	4	4	4	4
Cations	P	0.981	0.988	0.984	0.968	0.989	0.990	0.987	0.968	0.979	0.967	0.975	0.990	0.991	0.978	0.985
	Si	0.020	0.018	0.022	0.061	0.017	0.017	0.021	0.041	0.037	0.037	0.033	0.016	0.018	0.025	0.022
	ΣT-site	1.001	1.006	1.006	1.028	1.006	1.007	1.008	1.009	1.016	1.004	1.009	1.006	1.009	1.004	1.007
	Ca	0.052	0.040	0.048	0.037	0.034	0.037	0.044	0.060	0.045	0.069	0.060	0.033	0.039	0.052	0.049
	Y	0.052	0.041	0.047	0.034	0.038	0.040	0.039	0.043	0.042	0.054	0.050	0.040	0.043	0.042	0.042
	La	0.166	0.172	0.165	0.169	0.178	0.172	0.169	0.156	0.166	0.147	0.152	0.175	0.170	0.166	0.168
	Ce	0.411	0.428	0.415	0.427	0.438	0.433	0.424	0.398	0.418	0.376	0.392	0.436	0.426	0.414	0.414
	Pr	0.046	0.047	0.046	0.047	0.047	0.048	0.047	0.045	0.046	0.045	0.044	0.050	0.047	0.045	0.044
	Nd	0.158	0.163	0.162	0.166	0.168	0.168	0.162	0.158	0.160	0.152	0.156	0.169	0.165	0.159	0.161
	Sm	0.027	0.028	0.027	0.028	0.026	0.027	0.028	0.028	0.028	0.027	0.028	0.029	0.027	0.027	0.026
	Gd	0.020	0.018	0.019	0.020	0.018	0.020	0.017	0.018	0.018	0.024	0.021	0.019	0.020	0.020	0.020
	Pb	0.003	0.002	0.002	0.002	0.002	0.002	0.002	0.003	0.002	0.003	0.003	0.001	0.002	0.002	0.002
	Th	0.060	0.047	0.058	0.039	0.041	0.043	0.053	0.079	0.054	0.094	0.081	0.038	0.045	0.066	0.061
	U	0.007	0.005	0.005	0.004	0.004	0.004	0.004	0.004	0.004	0.005	0.004	0.004	0.004	0.004	0.004
	Σa-site	1.001	0.992	0.993	0.972	0.993	0.992	0.990	0.991	0.983	0.996	0.990	0.994	0.988	0.997	0.991
	% Hutt	1.97	1.76	2.14	5.87	1.66	1.69	2.10	4.04	3.63	3.66	3.30	1.58	1.81	2.49	2.21
	% Brab	12.00	9.27	10.84	8.22	7.87	8.30	10.00	13.05	10.07	15.22	13.37	7.55	8.86	11.36	10.87
	% Mnz	86.03	88.97	87.02	85.91	90.47	90.01	87.90	82.91	86.29	81.12	83.33	90.87	89.33	86.14	86.92

Indeed, in the latter, the lack of zircon grains is possibly leading to a buffering of Zr content in the minerals inducing an underestimation of temperatures. Two zirconium isotopes (^{90}Zr and ^{91}Zr) have been analyzed. Their respective Zr concentrations in the ablated grains are similar within error. The differences between the two isotopes concentrations for a same ablation spot range from 0 to ca. 4%. This difference of concentration leads to a difference in the computation of the temperature ranging from 0 to 0.99%. Considering the uncertainty of the thermometer which was estimated by Zack et al. (2004a) at ±50 °C, we assume that using the concentration of one isotope or the other does not affect significantly the results. Thus, computation of temperatures is based on the most abundant zirconium isotope content: ^{90}Zr.

Crystallization temperatures of rutile grains from kyanite-micaschists (samples CHI0999#93-17-a and -b) from the two different generations are reported in Fig. 14b and Table 5. Rutile associated with the S_3 schistosity display temperatures ranging from 580 to 620 ± 50 °C (Syn-D_{2-3}, Fig. 14b). Rutile grains associated with sulfides and shear bands marking late-D_3 metamorphic stage display temperatures ranging from 540 to 610 ± 50 °C (Late-D_3, Fig. 14b).

In addition, thermometric constraint was obtained in garnet-micaschists by garnet–phlogopite (Grt–Phl) thermometry based on Fe–Mg contents of crystal rims along garnet–phlogopite grain contacts (Holdaway, 2000). In the Lumwana's micaschists, phlogopite delineating the S_3 schistosity in textural equilibrium with garnet poikiloblasts record temperatures ranging from 630 to 635 ± 25 °C (Table 6) at 6 kbar (minimum pressure recorded for D_3 metamorphic stage by Eglinger et al., in press). Temperatures computed for 9 and 12 kbar are similar to the ones obtained for 6 kbar (temperature differences do not exceed 3 °C, Table 6).

7. Discussion

7.1. Metamorphic evolution recorded by the Lumwana micaschists

Results from the present study and data from literature are summarized in a *P–T* diagram in which the evolution of the microstructures and paragenesis of the Lumwana's Cu-rich kyanite-micaschists are reported (Fig. 15).

In the present study, we have identified three deformation stages marked by distinct mineral assemblages and microstructures. The first deformation stage, D_1, marked by Ky_1 poikiloblasts containing a relictual $S_{0/1}$ foliation delineated by oriented mineral inclusions of micas, graphite and Cu-sulfides (a bornite-rich/chalcopyrite-poor assemblage), is interpreted to represent the metamorphic paragenesis developed during the prograde part of the *P–T* path. The metamorphic peak assemblage characterized by a Ky_1 and graphite assemblage, records HP–MT conditions (D_1 deformation-metamorphic stage, Fig. 15) as proposed by Eglinger et al. (in press) and John et al. (2004). This HP–MT D_1 event is attributed to burial down to 40–50 km under a geothermal gradient of 15–20 °C·km^{-1} related to subduction of the continental margin of the Congo craton at ca. 550–530 Ma (John et al., 2004; Eglinger et al., 2014b) followed by the collision of the Congo and Kalahari cratons (John et al., 2004; Eglinger et al., in press). In the Solwezi region, kilometer-scale isoclinal folds might be attributed to this D_1 phase (Cosi et al., 1992; Eglinger et al., in press).

The second deformation stage, D_2, is marked by a steep-dipping schistosity S_2, delineated by the preferred orientation of phlogopite and muscovite (001) cleavage planes wrapped around late-D_1 porphyroblasts of plagioclase. At the regional scale, in the Solwezi region, the F_1 isoclinal folds are refolded by asymmetric F_2 folds resulting with hook-type interferences consistent with a top-to-the south sense of shear (Cosi et al., 1992; Eglinger et al., in press). The S_2 schistosity also includes a second generation of Cu sulfides (chalcopyrite–pyrrhotite) and a second generation of kyanite porphyroblasts (Ky_2) locally kinked and wrapped by the later S_3 schistosity. These textural observations lead us to propose that these porphyroblasts have developed during D_2 metamorphic stage and have recrystallized during D_3 metamorphic stage and are thus denominated as Ky_{2-3} porphyroblasts. Similarly, some monazite grains aligned with relics of the S_2 schistosity (see Section 5.4.2.) are interpreted as developed during the D_2 metamorphic stage. In garnet-micaschists, the onset of the crystallization of garnet poikiloblasts is attributed to this metamorphic stage. The *P–T* conditions recorded by the S_2 mineral paragenesis indicate an isothermal decompression from ca. 620 to 580 °C. These structural and metamorphic data are interpreted to record syn-orogenic exhumation.

The final deformation stage, D_3, is marked by the transposition of the steep-dipping S_2 schistosity in a shallow-dipping S_3 schistosity, by the kinking and recrystallization of the second generation of sub-automorphous kyanite (designated as Ky_{2-3}), a third generation of Cu sulfides (chalcopyrite and bornite), monazite and rutile grains oriented parallel to the (001) cleavage plane of associated micas defining the shallow-dipping S_3 schistosity. Most of the crystallization of syn-D_{2-3} garnet poikiloblasts is attributed to this metamorphic paragenesis. Zr-in-rutile geothermometry data obtained on rutile grains oriented parallel to the (001) cleavage plane of syn-S_3 micas lead to the computation of temperatures between 580 and 620 ± 50 °C (Syn-D_{2-3}, Figs. 14b and 15, Table 5). This range of temperatures corresponds to those estimated by Eglinger et al. (in press) for the development of the steep-dipping schistosity (S_2) in the internal zone of the Lufilian belt (P = 6–8 kbar; T = 600–640 °C). As the rutile grains analyzed for Zr-in-rutile geothermometry delineate the shallow-dipping S_3 schistosity but display temperatures consistent with the development of the steep-dipping S_2 schistosity, we propose that these rutile grains record the development of the D_2 paragenesis between 580 and 620 ± 50 °C (Syn-D_{2-3}, Figs. 14b and 15, Table 5) and have been transposed in the S_3 schistosity. These MP–MT conditions and the steep-dipping fabrics have been attributed to the D_2 syn-orogenic exhumation of high-grade metamorphic rocks, due to tectonic accretion of subducted continental units decoupled from the down-going slab. Even though the garnet-phlogopite equilibrium is coeval with the development of the S_3 schistosity, it records temperatures from 630 to 635 ± 25 °C (Table 6) at 6 kbar (minimum pressure recorded for this stage by Eglinger et al., in press; see Section 6.2. for details), which are higher than those obtained by Zr-in-rutile geothermometry in the present study and which record the emplacement of the D_2 metamorphic paragenesis between 580 and 620 ± 50 °C. This difference might result from (i) a thermodynamic disequilibrium between garnet, which might have preserved its syn-D_2 chemical composition, and syn-D_3 phlogopite; or (ii) an augmentation of temperature between D_2 and D_3 metamorphic stages due to a heat production during thermal relaxation in the thickened orogenic crust induced by the radioactive decay of radioisotopes (cf. Vanderhaeghe, 2012). However, an augmentation of temperature between D_2 and D_3 metamorphic stages is not reported in the estimations of Eglinger et al. (in press) or in the present study where there is no evidence of such an augmentation between D_2 and D_3 metamorphic paragenesis or in the temperatures recorded by rutile grains.

Monazite grains in Lumwana's Cu-rich kyanite-micaschists associated with relics of the S_2 schistosity and locally transposed and partially recrystallized during the D_3 metamorphic event yield ^{208}Pb/^{232}Th ages ranging from 537.1 ± 6.6 down to 502.8 ± 6.3 Ma (Fig. 13b, see Section 5.4.2 for details, Fig. 10). The scattering of these ages (Fig. 13c) is interpreted as recording decompression coeval with ductile deformation, i.e. monazite grains crystallized during a continuum of deformation from the initiation of the D_2 metamorphic stage around ca. 540 Ma down to the end of the D_3 deformation stage in the kyanite stability field (Ky_{2-3}) at ca. 500 Ma. Data from literature constrain the peak of metamorphism (designated in the present study as D_1 event) at ca. 550–530 Ma (Eglinger et al., 2014b, in press; John et al., 2004). The ^{208}Pb/^{232}Th ages obtained in the present study on syn- to late-metamorphic monazite grains fall within the margins of the D_1 stage constraints and probably record the retrograde clockwise *P–T* path from the D_2 to the D_3 metamorphic stages.

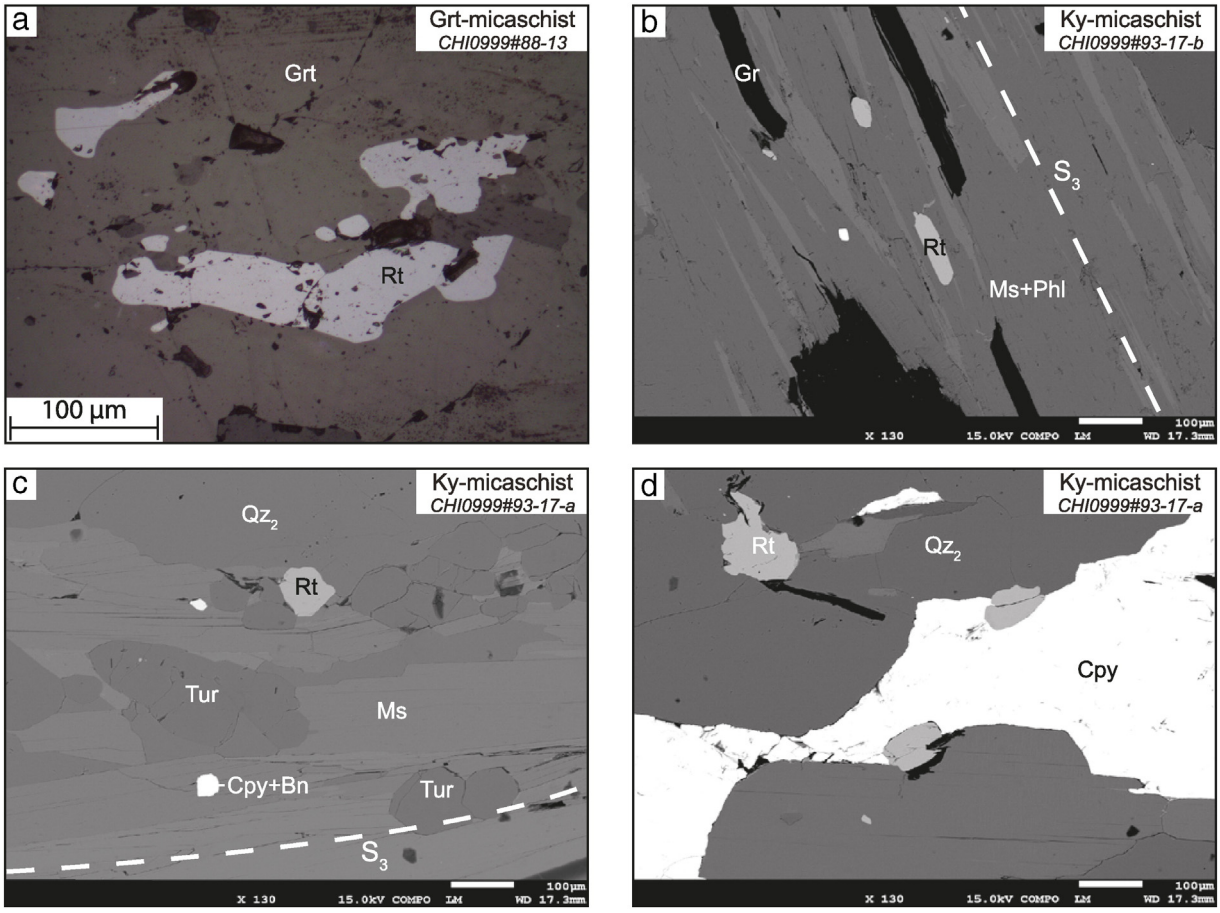

Fig. 11. Photomicrographs illustrating the structural position of rutile grains and their relationship with the mineralization and the matrix from samples CHI0999#88-13, 93-17-a and 17-b. a: rutile grains enclosed into a syn-S_3 poikiloblast of garnet (reflected light); b: rutile grains delineating the S_2 fabric and synchronous with graphite (SEM); c: late-D_3 rutile grain associated with tourmaline crystals, marking the retrograde part of the *P-T* path (SEM); d: rutile grains associated with mineralization (SEM). Abbreviations: Bn = bornite; Cpy = chalcopyrite; Gr = graphite; Grt = garnet; Ms = muscovite; Phl = phlogopite; Qz_2 = second generation of quartz; Rt = rutile; Tur = tourmaline.

This D_3 deformation stage is ended by C_3 shear bands marked by retrogression of phlogopite into chlorite (Fig. 8f). These shear bands (i) crosscut all previous metamorphic fabrics, (ii) are associated with the formation of euhedral pyrite and tourmaline crystals and (iii) locally remobilize Cu sulfides. This late-D_3 event is interpreted as the expression of post-orogenic gravitational collapse coeval with cooling of the high-grade metamorphic nappes of the Lufilian orogenic belt (D_3 deformation-metamorphic stage, Fig. 15). This is further corroborated by the temperature from 610 down to 540 ± 50 °C yielded by rutile grains associated with remobilized sulfides and shear bands associated with the late-D_3 metamorphic fabrics development (Late-D_3, Fig. 14b, Table 5). No monazite grains crystallized during this late deformation stage, which is interpreted as postdating these minerals. We thus propose that the late-D_3 fabric development is younger than ca. 500 Ma, the youngest U–Th–Pb age obtained on monazite. This is in good agreement with the onset of cooling of the metamorphosed

Table 4
Representative rutile analyses from samples CHI0999#88-13, 93-17-a & -17-b obtained using LA-ICP-MS. ^{47}Ti was used as internal standard, using [TiO_2] = 100 wt.%. Abbreviation: Syn-D_{2-3} = syn-D_2 rutile grains transposed in D_3 fabrics.

Sample		88-13	88-13	88-13	88-13	88-13	88-13	93-17-a	93-17-b	93-17-b	93-17-b	93-17-b	93-17-b	93-17-b	93-17-b
Analysis no.		8	9	10	11	12	13	14	15	16	17	19	20	21	22
Structural position		Pre-D_3	Pre-D_3	Pre-D_3	Pre-D_3	Pre-D_3	Pre-D_3	Syn-D_{2-3}	Syn-D_{2-3}	Syn-D_{2-3}	Syn-D_{2-3}	Syn-D_{2-3}	Syn-D_{2-3}	Syn-D_{2-3}	Syn-D_{2-3}
Elements (ppm)	^{53}Cr	65	84	74	78	80	80	472	512	470	329	429	430	506	526
	^{90}Zr	59	70	74	66	70	70	116	106	100	98	112	140	133	135
	^{91}Zr	59	72	73	65	67	71	114	109	100	99	110	142	131	136
	^{93}Nb	2400	5650	5440	4670	3720	4510	6230	5330	4760	3470	5850	7300	6410	6150

Sample		93-17-a	93-17-a	93-17-a	93-17-a	93-17-a	93-17-a	93-17-a	93-17-a	93-17-a	93-17-a	93-17-a	93-17-a	93-17-a
Analysis no.		23	24	25	26	27	28	29	2	3	4	5	6	7
Structural position		Syn-D_{2-3}	Syn-D_{2-3}	Syn-D_{2-3}	Syn-D_{2-3}	Syn-D_{2-3}	Syn-D_{2-3}	Syn-D_{2-3}	Late-D_3	Late-D_3	Late-D_3	Late-D_3	Late-D_3	Late-D_3
	^{53}Cr	369	377	389	397	398	429	458	394	359	393	401	351	383
	^{90}Zr	106	114	112	113	101	121	134	121	125	120	125	76	117
	^{91}Zr	103	113	114	113	101	122	135	121	124	121	125	77	117
Elements (ppm)	^{93}Nb	3950	3850	5170	4810	4600	5350	5980	5109	4430	5625	5684	3390	4640

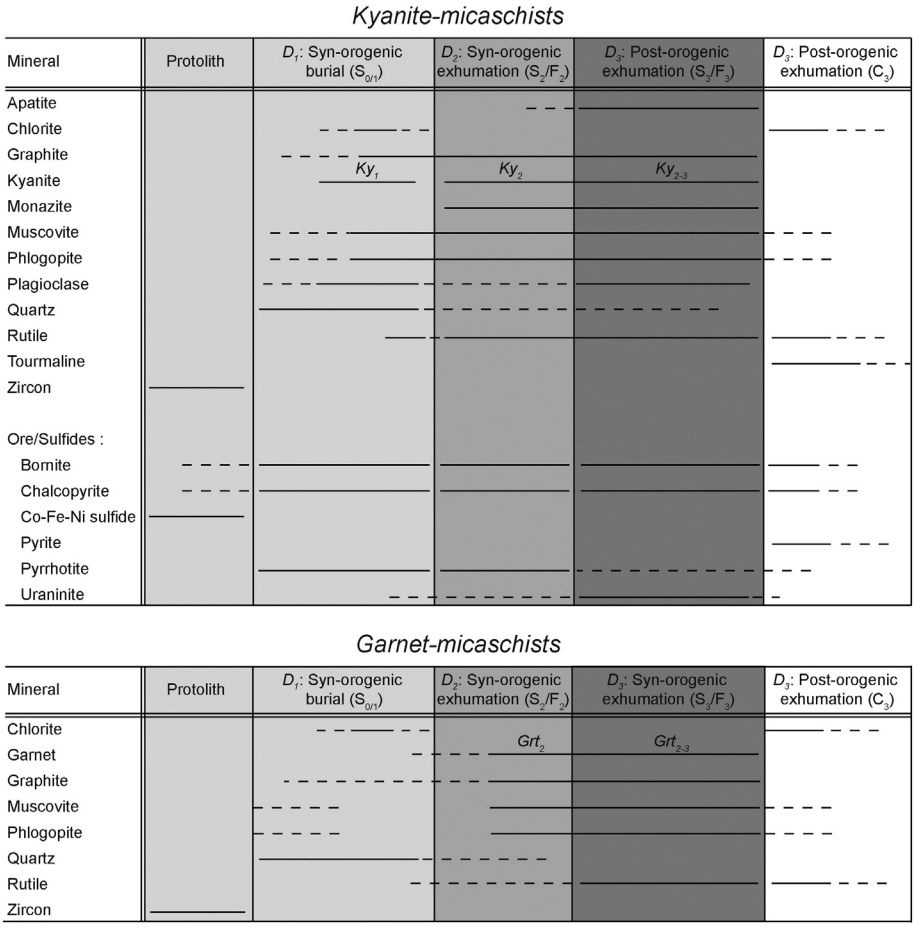

Fig. 12. Paragenetic sequence of garnet- and kyanite-micaschists from the Lumwana deposit (Mwombezhi dome).

rocks reported in the literature which constrain this stage between ca. 500 and 470 Ma (Rb–Sr isotopic ages on muscovite and biotite; see Section 2.1 for details, Cosi et al., 1992; John et al., 2004).

7.2. Successive syn-metamorphic remobilization of Lumwana's mineralization during Pan-African orogeny

In micaschists from Chimiwungo, pyrrhotite and bornite grains are not present in the same sections of the studied micaschists. The lower part of the drill core presents bornite associated with chalcopyrite grains whereas the upper part contains a chalcopyrite–pyrrhotite (± pyrite) assemblage. These two assemblages are mutually exclusive as described by Benham et al. (1976), Bernau (2007) and Bernau et al. (2013).

In the present study, we identified three Cu sulfide generations in kyanite-micaschists from Chimiwungo that are interpreted as being related to distinct mineralizing events. The first generation of sulfides is represented as chalcopyrite–pyrrhotite or chalcopyrite–bornite (a bornite-rich/chalcopyrite-poor assemblage) as inclusions into Ky_1 (Fig. 8b). This is consistent with the observations of Benham et al. (1976), Bernau (2007) and Bernau et al. (2013) who proposed the presence of Cu in the protolith of the micaschists prior to the peak of metamorphism.

The second generation of sulfides, marked by a chalcopyrite-pyrrhotite (sample CHI0999#89-16-b) or chalcopyrite-bornite assemblage (sample CHI0999#93-17-a), is coeval with the development of a second steep-dipping S_2 schistosity, initiating the retrograde *P–T* path (D_2 metamorphic event), and a second generation of kyanite porphyroblasts later transposed in the S_3 schistosity (Ky_{2-3} porphyroblasts).

The third and final generation of sulfides described in the present study is coeval with the kinking and partial recrystallization of a second generation of kyanite (Ky_{2-3}) marking the third metamorphic assemblage identified, corresponding to the retrograde part of the *P–T* path (D_3 metamorphic event). In addition, Cu sulfides (a bornite-poor/chalcopyrite-rich assemblage) are expressed as pressure shadows around Ky_1 grains, which are porphyroclasts wrapped in the S_3 schistosity. In some cases, these sulfides may fill fractures present in Ky_1 (Fig. 7), but are not fully enclosed into the aluminosilicates.

Benham et al. (1976), Bernau (2007) and Bernau et al. (2013) described a local remobilization of sulfides during metamorphism, with no addition of copper, as chalcopyrite and bornite can be found in pressure shadows of kyanite porphyroblasts. However, these authors considered only one generation of kyanite around which pressure shadows contain Cu sulfides. In addition, they do not specify if the presence of Cu is related to diagenetic or hydrothermal processes (Benham et al., 1976; Bernau, 2007; Bernau et al., 2013).

Textural evidence show that Ky_1 porphyroblasts first crystallized during the development of the $S_{0/1}$ foliation (D_1 deformation-metamorphic stage, Fig. 15) as a witness of the metamorphic peak and were fractured during the development of the retrograde S_3 schistosity (D_3 deformation-metamorphic stage), before being filled in by Cu sulfides (Fig. 7). In these pressure shadows (sample CHI0999#93-17-b), monazite grains are enclosed or co-genetic to the sulfide assemblage and to the S_3 schistosity. Monazite fully enclosed in the syn-D_3 sulfide assemblage displays $^{208}Pb/^{232}Th$ ages ranging from 525.8 ± 6.8 Ma to 511.2 ± 6.6 Ma (Fig. 10c, Table 1). These ages are bracketed into the time period recorded by the other monazite grains, which are co-genetic (i) with the syn-D_3 mineralization and (ii) with the development of the S_2 and S_3 schistosities, and which display $^{208}Pb/^{232}Th$ ages

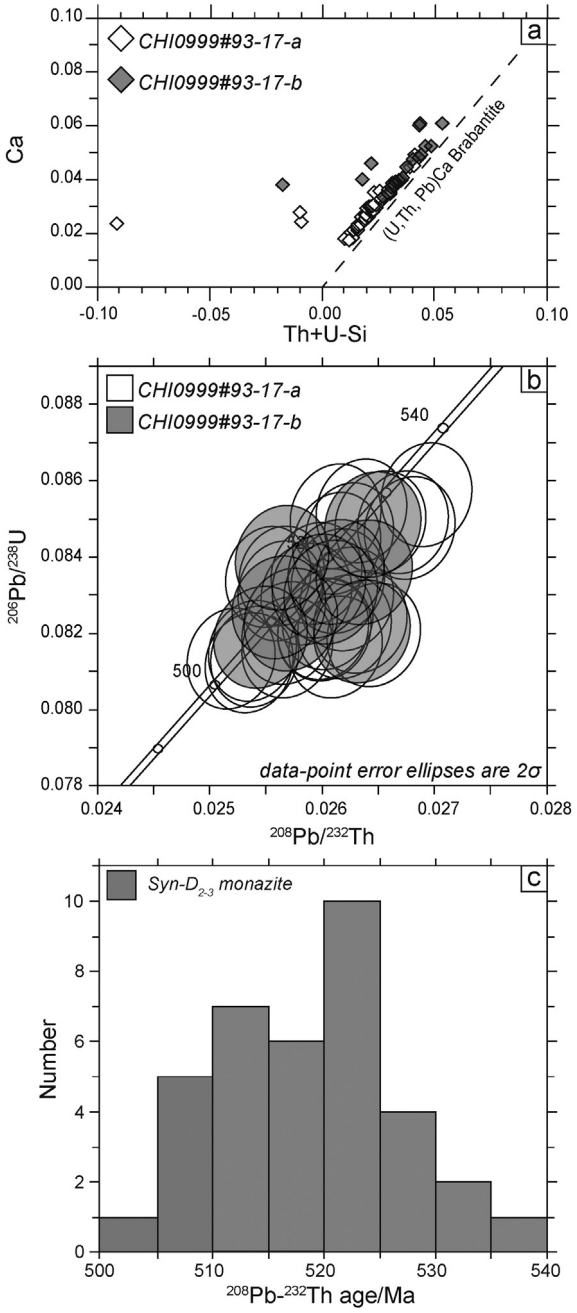

Fig. 13. Geochemical signatures and $^{208}Pb/^{232}Th$ ages of syn-S_3 monazite grains from CHI0999#93-17-a and 17-b from Lumwana. a: Ca vs Th + U - Si diagram showing the relative proportions of brabantite substitutions in monazite end-members; b: Concordia plots of U-Th-Pb data (n = 28 in sample CHI0999#93-17-a, n = 10 in sample CHI0999#93-17-b, data-point error ellipses are 2σ); c: Histogram of Pan-African monazite $^{208}Pb/^{232}Th$ ages from sample CHI0999#93-17-a and 17-b.

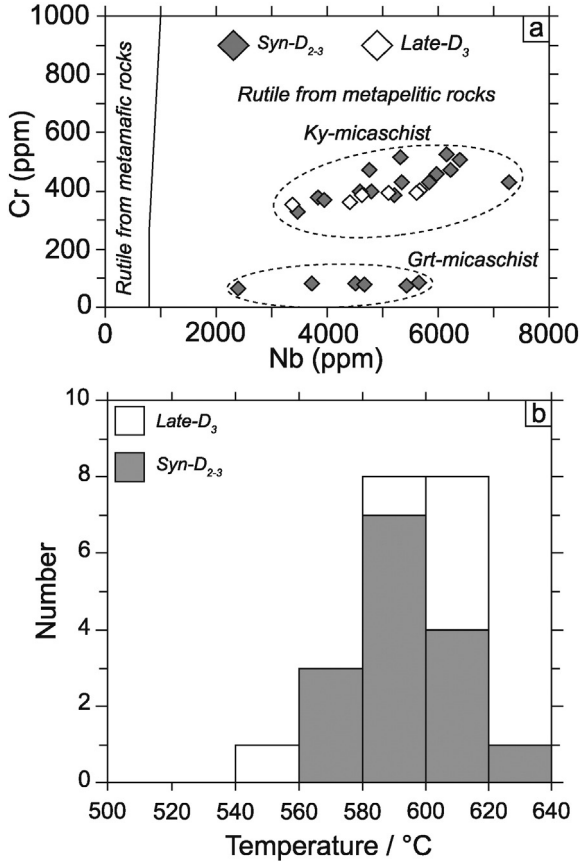

Fig. 14. Geochemical signatures of rutile grains and Zr-in-rutile geothermometry of samples CHI0999#93-17-a and 17-b from Lumwana. a: Cr vs Nb content diagram constraining the crystallization environments of rutile (after Zack et al., 2004b; Triebold et al., 2007; Meinhold et al., 2008); b: rutile crystallization temperature obtained using Zr-in-rutile thermometry defined by Zack et al. (2004a). Analyzes are reported in Table 4. Abbreviation: Syn-D_{2-3} = syn-D_2 rutile grains transposed in D_3 fabrics.

from 537.1 ± 6.6 Ma to 502.8 ± 6.3 Ma (Figs. 10). These new data evidence that a Cu mineralizing event developed during the whole D_3 phase in the kyanite stability field from ca. 540 Ma to ca. 500 Ma, i.e. during the syn- to post-orogenic exhumation of the high-grade metamorphic rocks forming the orogenic root of the Pan-African Lufilian belt (D_3 deformation-metamorphic stage, Fig. 15). This Cu mineralizing event overlaps with the U–Pb ages obtained on syn-metamorphic uraninite dated at 531 ± 5 Ma (Eglinger et al., in press) from kyanite-micaschists sampled in the same drill core, and overlap, within their uncertainty, the Re–Os ages ranging from 534.4 ± 2.2 to 524.8 ± 2.2 Ma obtained by Nowecki (2014) on syn-metamorphic molybdenite from the Lumwana deposit. This author proposes that the molybdenite is syn-metamorphic and that the ages obtained on this phase are coeval with the metamorphic peak Cu mineralization.

In addition to these textural observations and geochronological data, Eglinger et al. (2014a) described the circulation of $CaCl_2$–NaCl–KCl–($MgCl_2$) fluids in two uranium occurrences from the Western Zambian Copperbelt (Lolwa and Mitukuluku, Fig. 1), during a high-temperature (500–700 °C) syn-deformation stage of the Pan-African metamorphism of the Lufilian belt (Eglinger et al., 2014a, 2014b). The analysis of these fluid inclusions by LA-ICP-MS reveals (i) high U contents (from 1 to 570 $\mu g \cdot g^{-1}$ of U in the Lolwa occurrence and from 5 to 150 $\mu g \cdot g^{-1}$ in the Mitukuluku occurrence, Eglinger et al., 2014a) but also (ii) high Cu concentrations (from 1300 to 22,000 $\mu g \cdot g^{-1}$ of Cu in Lolwa and from 480 to 2300 $\mu g \cdot g^{-1}$ in Mitukuluku, Eglinger et al., 2014a). The fluid salinities are 53–59 mass% of $CaCl_2$ and 13–15 mass% of NaCl (Eglinger et al., 2014a). These authors propose that the high salinity of this mineralizing fluid is related to the dissolution of evaporites from the Lower Roan Group described in the Katanga sequence (Fig. 2). Moreover, the textural position of ore minerals at Lolwa and Mitukuluku indicates that they are associated with this U- and Cu-rich fluid circulation at ca. 530 Ma at minimum *P–T* conditions of ca. 5 kbar and 500 °C (Eglinger et al., 2014a, 2014b). As the Lumwana deposit displays similarities with the ones of Lolwa and Mitukuluku (mineralization hosted in kyanite-micaschists, upper amphibolite metamorphic facies recorded at ca. 550 Ma), and is located between these two localities, we propose that the highly-saline fluid described by Eglinger et al. (2014a) in the uranium occurrences of Lolwa and Mitukuluku have also circulated in the Mwombezhi Dome, in particular

Table 5
Zr-in-rutile thermometry for representative rutile grains from different structural positions from samples CHI0999#93-17-a & -17-b. Zr content was obtained using LA-ICP-MS. Abbreviation: Syn-D_{2-3} = syn-D_2 rutile grains transposed in D_3 fabrics.

Structural position	Sample	Analysis no.	Zr content		Zack et al. (2004a) thermometer	
			(ppm)	2σ	Temperature (°C)	Uncertainty
Syn-D_{2-3}	CHI0999#93-17-a	14	116	8	597	50
Syn-D_{2-3}	CHI0999#93-17-b	15	106	3	586	50
Syn-D_{2-3}	CHI0999#93-17-b	16	100	2	578	50
Syn-D_{2-3}	CHI0999#93-17-b	17	98	2	576	50
Syn-D_{2-3}	CHI0999#93-17-b	19	112	4	593	50
Syn-D_{2-3}	CHI0999#93-17-b	20	140	2	621	50
Syn-D_{2-3}	CHI0999#93-17-b	21	133	2	615	50
Syn-D_{2-3}	CHI0999#93-17-b	22	135	3	617	50
Syn-D_{2-3}	CHI0999#93-17-a	23	106	3	586	50
Syn-D_{2-3}	CHI0999#93-17-a	24	114	3	595	50
Syn-D_{2-3}	CHI0999#93-17-a	25	112	4	593	50
Syn-D_{2-3}	CHI0999#93-17-a	26	113	4	594	50
Syn-D_{2-3}	CHI0999#93-17-a	27	101	4	580	50
Syn-D_{2-3}	CHI0999#93-17-a	28	121	4	603	50
Syn-D_{2-3}	CHI0999#93-17-a	29	134	7	616	50
Late-D_3	CHI0999#93-17-a	2	121	2	603	50
Late-D_3	CHI0999#93-17-a	3	125	2	607	50
Late-D_3	CHI0999#93-17-a	4	120	2	602	50
Late-D_3	CHI0999#93-17-a	5	125	2	608	50
Late-D_3	CHI0999#93-17-a	6	76	1	544	50
Late-D_3	CHI0999#93-17-a	7	117	3	598	50

at Lumwana. All these features suggest that some syn-D_2 Cu and U elements are mobilized in the system by metamorphic fluids linked to the dissolution of evaporitic rocks. The metals transferred in these highly-saline fluids might originate from (i) an in-situ remobilization of an older sulfide stock already present in the host rocks, and/or (ii) another host rock. Whether the syn-orogenic remobilization of copper sulfides is related or not to a new input of metals during the Lufilian orogeny remains an open question. As textural evidence led us to conclude that some Cu was present in the protolith of the kyanite-micaschists before metamorphism, we propose that at least part of the syn-metamorphic Cu deposition occurred by remobilization of the host rocks and their preexisting sulfides assisted by the circulation of highly-saline metamorphic fluids during the Pan-African orogeny. Such an in-situ remobilization of Cu-sulfides during metamorphism with no addition of Cu is also proposed by Benham et al. (1976), Bernau (2007) and Bernau et al. (2013).

Table 6
Representative garnet and phlogopite analyses by EMP on sample CHI0999#88-13 and Fe-Mg thermometer results (Holdaway, 2000). Abbreviations: Grt = garnet; Phl = phlogopite.

Sample		88-13	88-13	88-13	88-13	88-13	88-13	88-13	88-13	88-13	88-13	88-13	88-13	88-13	88-13	88-13	88-13
Analysis no.		7	6	8	9	11	10	12	13	15	14	16	17	19	18	20	21
Mineral		Phl	Grt	Phl	Grt	Phl	Grt	Phl	Grt	Phl	Grt	Phl	Grt	Phl	Grt	Phl	Grt
		Rim	Rim	Rim	Rim	Rim	Rim	Rim	Rim	Rim	Rim	Rim	Rim	Rim	Rim	Rim	Rim
Oxides/ wt.%	SiO_2	36.44	37.36	36.13	36.55	36.09	37.36	36.73	37.50	36.49	37.46	35.31	36.92	35.75	36.95	35.98	37.57
	TiO_2	1.49	0.06	1.29	0.10	1.54	0.06	1.55	0.20	1.62	0.07	1.60	0.07	1.58	0.15	1.58	0.16
	Al_2O_3	19.11	21.05	18.77	20.62	18.89	20.74	18.90	20.88	18.85	20.72	18.76	20.67	18.78	20.83	18.97	20.53
	FeO	15.45	30.67	15.80	30.77	15.75	30.32	15.86	31.24	15.48	31.37	15.33	30.77	15.30	30.98	15.57	30.44
	MnO	0.00	1.66	0.08	2.31	0.00	2.12	0.09	2.00	0.17	2.22	0.03	1.91	0.12	2.28	0.15	2.17
	MgO	12.35	3.21	11.78	2.74	12.39	2.90	12.03	2.80	12.35	2.88	11.57	2.91	12.60	2.94	12.03	2.84
	CaO	0.00	4.50	0.08	4.40	0.01	4.44	0.03	4.50	0.02	4.18	0.78	4.21	0.06	4.37	0.01	4.20
	Na_2O	0.33	–	0.16	–	0.28	–	0.37	–	0.23	–	0.50	–	0.31	–	0.23	–
	K_2O	9.46	–	9.98	–	9.60	–	9.51	–	9.41	–	9.29	–	10.02	–	10.05	–
	Total	94.63	98.51	94.07	97.49	94.55	97.94	95.07	99.12	94.62	98.90	93.17	97.46	94.52	98.50	94.57	97.91
Oxygens		22	12	22	12	22	12	22	12	22	12	22	12	22	12	22	12
Cations	Si	5.469	3.010	5.488	3.000	5.440	3.029	5.499	3.016	5.480	3.025	5.412	3.016	5.405	2.999	5.437	3.045
	Al^{IV}	2.531	0.000	2.512	0.000	2.560	0.000	2.501	0.000	2.520	0.000	2.588	0.000	2.563	0.001	2.563	0.000
	Al^{VI}	0.849	2.002	0.848	1.995	0.797	1.986	0.835	1.982	0.817	1.973	0.801	1.993	0.815	1.990	0.815	1.966
	Ti	0.168	0.004	0.147	0.006	0.175	0.004	0.175	0.012	0.183	0.004	0.184	0.004	0.180	0.009	0.180	0.010
	Fe^{tot}	1.939	2.088	2.007	2.113	1.986	2.080	1.986	2.115	1.944	2.122	1.965	2.120	1.935	2.103	1.968	1.966
	Mn	0.000	0.113	0.010	0.161	0.000	0.146	0.011	0.136	0.022	0.152	0.004	0.132	0.015	0.157	0.018	0.149
	Mg	2.763	0.386	2.668	0.335	2.784	0.350	2.685	0.336	2.765	0.347	2.644	0.354	2.840	0.356	2.710	0.343
	Ca	0.000	0.388	0.013	0.387	0.002	0.386	0.005	0.388	0.003	0.362	0.128	0.368	0.010	0.380	0.002	0.365
	Na	0.096	–	0.047	–	0.082	–	0.107	–	0.067	–	0.149	–	0.091	–	0.067	–
	K	1.811	–	1.934	–	1.846	–	1.816	–	1.803	–	1.817	–	1.933	–	1.937	–
	X_{Mg}	0.59	0.13	0.57	0.11	0.58	0.12	0.57	0.11	0.59	0.12	0.57	0.12	0.59	0.12	0.58	0.12
	X_{Fe}	0.41	0.70	0.43	0.71	0.42	0.70	0.43	0.71	0.41	0.71	0.43	0.71	0.41	0.70	0.42	0.70
	X_{Mn}	–	0.04	–	0.05	–	0.05	–	0.05	–	0.05	–	0.04	–	0.05	–	0.05
	X_{Ca}	–	0.13	–	0.13	–	0.13	–	0.13	–	0.12	–	0.12	–	0.13	–	0.13
T/°C	6 kbar	633		633		635		632		632		631		633		635	
	9 kbar	634		634		636		633		633		633		635		636	
	12 kbar	635		635		637		635		634		634		636		637	

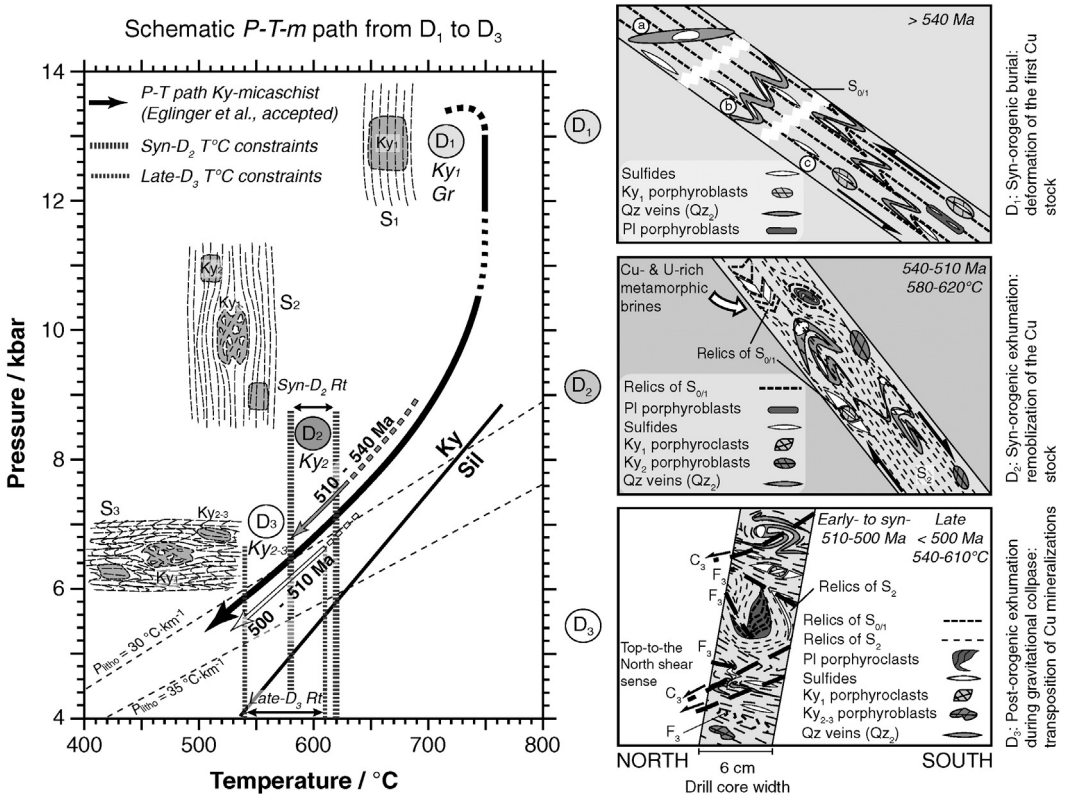

Fig. 15. Synthetic *P–T–m* diagram showing possible *P–T* path for Lumwana's Cu(–U)-rich kyanite-micaschists (black arrow) and their microstructural evolution during syn-orogenic burial (D_1), syn-orogenic exhumation (D_2), post-orogenic exhumation during gravitational collapse (late-D_3) during the Lufilian orogeny (see text for details; modified after Eglinger et al., in press). No constraints on the D_1 prograde part of the *P–T* path have been obtained in the present study, thus we chose to only represent the retrograde part of the *P–T* path (D_2 and D_3 events). Abbreviations: Gr = Graphite; Ky_1 = first generation of kyanite; Ky_2 = second generation of kyanite; Ky_{2-3} = second generation of kyanite transposed in the S_3 schistosity; Qz = quartz; Pl = plagioclase.

A final remobilization of sulfides occurred during the final stage of the retrograde *P–T* path during localized deformation in shallow-dipping shear zones (late-D_3 event). This late-D_3 phase postdates syn-D_3 monazite grains which yield youngest $^{208}Pb/^{232}Th$ ages of ca. 500 Ma. Accordingly the last remobilization of sulfides occurred during post-orogenic gravitational collapse and is younger than ca. 500 Ma (Fig. 15).

The correlation between mineralization and metamorphism leads to an assessment of the role of metamorphism in terms of concentration or dispersion of Cu. The mineralized paragenesis of the Lumwana's kyanite-micaschists during the Pan-African orogeny evolves from a bornite-rich (Cu_5FeS_4)/chalcopyrite-poor ($CuFeS_2$) assemblage inherited from the sedimentary protolith to a syn-metamorphic bornite-poor/chalcopyrite-rich assemblage developed during syn- and post-orogenic exhumation. This tends to show that the proportional abundance of Cu decreases (and Fe increases conversely) during metamorphism. This suggests that metamorphism may have a dispersive effect on Cu mineralization.

7.3. Nature of the protolith of the Lumwana micaschists

Micaschists from Chimiwungo display noticeable chemical variations. Indeed, within ten centimeters, the petrography varies from a kyanite- and sulfide-free garnet-rich micaschists to a garnet-free kyanite- and Cu-rich micaschists (Fig. 5). The mutual exclusivity of kyanite and garnet that both indicate the pressure conditions recorded by the samples, and the association of kyanite with the mineralization, may be related to a chemical difference inherited from the metasedimentary protolith. In addition, different generations of rutile have been identified (see Section 5.4.3) in kyanite-micaschists and in garnet-micaschists. The position of rutile from the Lumwana micaschists in the Cr vs Nb diagram (Fig. 14a), proposed by Zack et al. (2004b), Meinhold et al. (2008) and Triebold et al. (2007) point to a metapelitic environment of crystallization for all analyzed rutile grains. However, rutile from garnet-micaschists display a different Cr/Nb ratio compared to those from the kyanite-micaschists suggesting the chemical environment of rutile crystallization differed in these two distinct chemical layers which is consistent with a pre-metamorphic lithological compositional layering inherited from the sedimentary sequence. Furthermore, rounded zircon grains, enclosed into the quartz–plagioclase matrix and in micas delineating the S_1, S_2 and S_3 schistosities, suggest that they represent detrital grains inherited from a sedimentary protolith (Fig. 12). Similarly, Co–Fe–Ni sulfides grains show rounded shapes and evidence of alteration (Fig. 9a), consistent with a detrital origin. The most probable explanation for the presence of Ni in the system is that Co–Fe–Ni sulfides grains are detrital and come from the erosion of mafic intrusive bodies emplaced before the Pan-African orogeny. Some amphibolite boudins contained in the Chimiwungo hangingwall schist and in the core of the Mwombezhi dome (Fig. 4) display Nd model ages relative to the Depleted Mantle (T_{DM}) ranging from 2.93 to 2.32 Ga (Eglinger, 2013). They represent good candidates for the source of Ni.

Carbonaceous material is represented in the micaschists as graphite. This mineral may be hydrothermal or metamorphic in origin. The latter case implies that graphite crystallizes from organic matter during the prograde part of the *P–T* path and/or at the peak of metamorphism. Because graphite from the Chimiwungo micaschists is not associated with veins, suggesting a hydrothermal activity, we conclude that it probably has a metamorphic origin and records the D_1 peak of metamorphism. This is consistent with the elongation of graphite parallel to the (001) cleavage plane of the micas (Figs. 8e and 11b). Inclusions of graphite in Ky_1 evidence the presence of carbonaceous material in

the protolith of the micaschists before burial, i.e. before the D_1 metamorphic stage. All these arguments indicate that the protolith of the mineralized host rock at Lumwana (i.e. micaschists) is sedimentary, which is consistent with the proposition of Benham et al. (1976), and which complements the conclusions of Bernau (2007) and Bernau et al. (2013). Indeed, for the Lumwana Cu deposit, Bernau (2007) and Bernau et al. (2013) invoke a high metamorphic grade and pervasive deformation for the host rock of the mineralization with slivers of gneisses interleaved with micaschists, and a transitional contact between the gneiss and the ore schist. These observations led them to propose that the mineralization at the Lumwana deposit might be hosted in the basement of the Lower Roan. However, they do not precise if the protolith of the Cu-bearing micaschists is sedimentary or magmatic in origin. Even though we can conclude a sedimentary origin for Lumwana's kyanite-micaschists, no evidence allows us to conclude that these metasediments are part of the Katanga metasedimentary sequence or of its basement.

The identification of several generations of Cu sulfides leads to the following hypotheses: (i) an in-situ syn-tectonic remobilization with no addition of metals or (ii) a new input of metals during the Pan-African orogeny. Two lines of evidences argue in favor of in-situ remobilization: (i) Cu-bearing minerals are present in the non-metamorphic external zone (i.e. Congolese Copperbelt) and are also present as inclusions in porphyroclasts indicating that at least some Cu was present in the protolith of the kyanite-micaschists (i.e. oreschists) before metamorphism; and (ii) isotopic data (Lu/Hf) obtained by Eglinger (2013) indicates that the rocks of the Zambian Copperbelt are mostly originating from reworked Neo-Archean and Paleoproterozoic rocks with a minor Neoproterozoic input. However, if these sediments are part of the basement of the Katanga metasedimentary sequence, the metamorphic metal-rich brines circulation identified by Eglinger et al. (2014a), which originates from the dissolution of the Roan evaporites, might represent a new input of metals during the Lufilian orogeny. Even though an in-situ remobilization of Cu-sulfides during metamorphism with no addition of Cu is proposed by Benham et al. (1976); Bernau (2007) and Bernau et al. (2013), we cannot bring any evidence to exclude a new input of metals during the Lufilian orogeny.

Accordingly, the data presented in this paper on the Lumwana Cu deposit (Western Zambian Copperbelt) are consistent with a Cu deposit formed by (i) a primary mineralization stage marked by the crystallization of sulfides related to hydrothermal fluids during diagenesis leading to the formation of sediment-hosted stratiform deposits and (ii) a remobilization, with some dispersion, of this initial Cu metal stock associated with intracrystalline deformation, during the Pan-African deformation, metamorphism and metasomatism, assisted by the circulation of highly-saline fluids. A long and continuous remobilization of sulfides has occurred during the retrograde clockwise *P–T* path, first during syn-orogenic exhumation (ca. 540–510 Ma), then during post-orogenic exhumation (ca. 510–500 Ma) accommodated by pervasive ductile deformation in the kyanite stability field, and finally during late post-orogenic exhumation associated with localized shallow-dipping shear zones (younger than ca. 500 Ma). These successive tectonic phases recorded by the Lufilian belt, namely burial, syn-orogenic exhumation and post-orogenic exhumation, are typical of Phanerozoic orogenic belts (e.g. Vanderhaeghe, 2012 and references therein).

8. Conclusion

In the present study, we show that Cu(–U) mineralization in the Lumwana deposit is hosted by kyanite-micaschists, derived from remobilization of former siliciclastic sedimentary rocks, and marked by intracrystalline deformation and metamorphism reaching the upper amphibolite facies during the Pan-African orogeny. The presence of Cu sulfides associated with graphite as inclusions in kyanite poikiloblasts demonstrate that Cu was present in the protolith before it reaches peak of metamorphism. Sulfides delineating the S_1 schistosity together with a first generation of kyanite (Ky_1) indicate that this initial Cu stock was remobilized during burial of the metasediments. Sulfides are further remobilized during D_2 and then D_3, marked by Ky_{2-3} recording the retrograde part of the *P–T* path from ca. 620 down to 580 °C (rutile thermometry) and dated from ca. 540 to ca. 500 Ma (ages on monazite grains synchronous with the Cu mineralization). This syntectonic crystallization of Cu (and U) is interpreted to be contemporaneous with the circulation of metamorphic metal-rich brines. Final remobilization of the Cu sulfides occurred along shallow-dipping localized shear bands attributed to post-orogenic gravitational collapse of the metamorphic rocks. These textures are younger than ca. 500 Ma and are recorded from ca. 610 to 540 °C (late-D_3 rutile thermometry constraining this metamorphic event). All these features suggest that the Lumwana Cu deposit corresponds to a former sediment-hosted stratiform Cu deposit metamorphosed under upper amphibolite facies conditions. A primary diagenetic sulfide stock has been remobilized during the successive stages of Pan-African deformation and metamorphism from burial, tectonic accretion and gravitational collapse.

Acknowledgments

This work has been supported by CNRS (Centre National de la Recherche Scientifique) scientific national program NEEDS through the project on Mining and Chemical processes, co-founded by CEA and AREVA. The authors would like to thank Barrick Ltd. for providing access to Chimiwungo drill cores. The authors are grateful to Sandrine Mathieu (SEM), Lise Salsi (SEM) and Olivier Rouer (EMP) (GeoRessources, Nancy) for technical support in providing analytical data on SEM and EMP. The authors also thank Bruce Eglington and Philippe Muchez for careful review and Franco Pirajno for editorial handling that helped to improve the paper. We would also like to acknowledge the stimulating discussions with Régine Mosser-Ruck and Alexandre Tarantola.

References

Armstrong, R.A., Master, S., Robb, L.J., 2005. Geochronology of the Nchanga Granite, and constraints on the maximum age of the Katanga Supergroup, Zambian Copperbelt. J. Afr. Earth Sci. 42, 32–40.

Ballouard, C., Boulvais, P., Poujol, M., Gapais, D., Yamato, P., Tartèse, R., Cuney, M., 2015. Tectonic record, magmatic history and hydrothermal alteration in the Hercynian Guérande leucogranite, Armorican Massif, France. Lithos 220–223, 1–22.

Barra, F., Broughton, D., Ruiz, J., Hitzman, M., 2004. Multi-stage mineralization in the Zambian Copperbelt based on Re–Os isotope constraints. Denver Annual Meeting (November 7–10, 2004).

Batumike, M.J., Cailteux, J.L.H., Kampunzu, A.B., 2007. Lithostratigraphy, basin development, base metal deposits, and regional correlations of the Neoproterozoic Nguba and Kundelungu rock successions, central African Copperbelt. Gondwana Res. 11, 432–447.

Benham, D.G., Greig, D.D., Vink, B.W., 1976. Copper occurrences of the Mombezhi Dome Area, Northwestern Zambia. Econ. Geol. 71, 433–442.

Bernau, R., 2007. The Geology and Geochemistry of the Lumwana Basement Hosted Copper–Cobalt (Uranium) Deposits. University of Southampton, NW Zambia (PhD Thesis, 187 pp.).

Bernau, R., Roberts, S., Richards, M., Nisbet, B., Boyce, A., Nowecki, J., 2013. The geology and geochemistry of the Lumwana Cu (±Co ± U) deposits, NW Zambia. Mineral. Deposita 48, 137–153.

Brems, D., Muchez, P., Sikazwe, O., Mukumba, W., 2009. Metallogenesis of the Nkana copper–cobalt South Orebody, Zambia. J. Afr. Earth Sci. 55, 185–196.

Cailteux, J.L.H., Kampunzu, A.B., Lerouge, C., Kaputo, A.K., Milesi, J.P., 2005. Genesis of sediment-hosted stratiform copper–cobalt deposits, central African Copperbelt. J. Afr. Earth Sci. 42, 134–158.

Cailteux, J.L.H., Kampunzu, A.B., Lerouge, C., 2007. The Neoproterozoic Mwashya–Kansuki sedimentary rock succession in the central African Copperbelt, its Cu–Co mineralisation, and regional correlations. Gondwana Res. 11, 414–431.

Capistrant, P.L., Hitzman, M.W., Wood, D., Kelly, N.M., Williams, G., Zimba, M., Kuiper, Y., Jack, D., Stein, H., 2015. Geology of the enterprise hydrothermal nickel deposit, North-Western Province, Zambia. Econ. Geol. 110, 9–38.

Cosi, M., De Bonis, A., Gosso, G., Hunziker, J., Martinotti, G., Moratto, S., Robert, J.P., Ruhlman, F., 1992. Late Proterozoic thrust tectonics, high-pressure metamorphism and uranium mineralization in the Domes Area, Lufilian Arc, northwestern Zambia. Precambrian Res. 58, 215–240.

Cross, M.M., 1999. Rates and Mechanisms of Thermochemical Sulphate Reduction. University of Manchester (PhD Thesis, 313 pp.).

De Swardt, A.M.J., Drysdall, A.R., 1964. Precambrian geology and structure in central Northern Rhodesia. Mem. Geol. Surv. India North Rhod. 2 (87 pp.).

De Waele, B., Johnson, S.P., Pisarevsky, S.A., 2008. Palaeoproterozoic to Neoproterozoic growth and evolution of the eastern Congo Craton: its role in the Rodinia puzzle. Precambrian Res. 160, 127–141.
Decrée, S., Deloule, E., De Putter, T., Dewaele, S., Mees, F., Yans, J., Marignac, C., 2011. SIMS U–Pb dating of uranium mineralization in the Katanga Copperbelt: constraints for the geodynamic context. Ore Geol. Rev. 40, 81–89.
Dewaele, S., Muchez, P., Vets, J., Fernandez-Alonzo, M., Tack, L., 2006. Multiphase origin of the Cu–Co ore deposits in the western part of the Lufilian fold-and-thrust belt, Katanga (Democratic Republic of Congo). J. Afr. Earth Sci. 46, 455–469.
Dill, H.G., 2010. The "chessboard" classification scheme of mineral deposits: mineralogy and geology from aluminum to zirconium. Earth Sci. Rev. 100, 1–420.
Eglinger, A., 2013. Cycle de l'uranium et évolution tectono-métamorphique de la ceinture orogénique Pan-Africaine du Lufilien (Zambie). Thèse de doctorat de l'Université de Lorraine (395 pp.).
Eglinger, A., André-Mayer, A.S., Vanderhaeghe, O., Mercadier, J., Cuney, M., Decrée, S., Feybesse, J.L., Milesi, J.P., 2013. Geochemical signatures of uranium oxides in the Lufilian belt: from unconformity-related to synmetamorphic uranium deposits during the Pan-African orogenic cycle. Ore Geol. Rev. 54, 197–213.
Eglinger, A., Ferraina, C., Tarantola, A., André-Mayer, A.S., Vanderhaeghe, O., Boiron, M.C., Dubessy, J., Richard, A., Brouand, M., 2014a. Hypersaline fluids generated by high-grade metamorphism of evaporites: fluid inclusion study of uranium occurrences in the Western Zambian Copperbelt. Contrib. Mineral. Petrol. 167, 967–994.
Eglinger, A., Tarantola, A., Durand, C., Ferraina, C., Vanderhaeghe, O., André-Mayer, A.S., Paquette, J.L., Deloule, E., 2014b. Uranium mobilization by fluids associated with Ca–Na metasomatism: a *P–T–t* record of fluid–rock interactions during Pan-African metamorphism (Western Zambian Copperbelt). Chem. Geol. 386, 218–237.
Eglinger, A., Vanderhaeghe, O., André-Mayer, A.S., Goncalves, P., Zeh, A., Durand, C., Deloule, E., 2015. Tectono-metamorphic evolution of the internal zone of the Pan-African Lufilian orogenic belt (Zambia): implications for crustal reworking and syn-orogenic uranium mineralizations. Lithos, http://dx.doi.org/10.1016/j.lithos.2015.10.021 (in press).
El Desouky, H., Muchez, P., Cailteux, J., 2009. Two Cu–Co sulfide phases and contrasting fluid systems in the Katanga Copperbelt, Democratic Republic of Congo. Ore Geol. Rev. 36, 315–332.
Gasquet, D., Bertrand, J.-M., Paquette, J.-L., Lehmann, J., Ratzov, G., Guedes, R.D.A., Tiepolo, M., Boullier, A.-M., Scaillet, S., Nomade, S., 2010. Miocene to Messinian deformation and hydrothermal activity in a pre-Alpine basement massif of the French western Alps: new U–U–Th–Pb and argon ages from the Lauzière massif. Bull. Soc. Geol. Fr. 181, 227–241.
Hanson, R.E., Wilson, T.J., Munyanyiwa, H., 1994. Geologic evolution of the Neoproterozoic Zambezi Orogenic Belt in Zambia. J. Afr. Earth Sci. 18 (2), 135–150.
Hitzman, M.W., Kirkham, R., Broughton, D., Thorson, J., Selley, D., 2005. The sediment-hosted stratiform copper ore system. Economic Geology 100th Anniversary Volume, pp. 609–642.
Hitzman, M.W., Selley, D., Bull, S., 2010. Formation of sedimentary rock-hosted stratiform copper deposits through Earth history. Econ. Geol. 105, 627–639.
Hitzman, M.W., Broughton, D., Selley, D., Woodhead, J., Wood, D., Bull, S., 2012. The Central African Copperbelt: diverse stratigraphic, structural and temporal settings the world's largest sedimentary copper district. In: Hedenquiest, J.W., Harris, M., Camus, F. (Eds.), 2012. Geology and Genesis of Major Copper Deposits and Districts of the World. A tribute to Richard H Sillitoe, Society of Economic Geologists, special publication 16, pp. 487–514.
Holdaway, M.J., 2000. Application of new experimental and garnet Margules data to the garnet–biotite geothermometer. Am. Mineral. 85, 881–892.
John, T., Schenk, V., Haase, K., Scherer, E., Tembo, F., 2003. Evidence for a Neoproterozoic ocean in south-central Africa from mid-oceanic-ridge-type geochemical signatures and pressure–temperature estimates of Zambian eclogites. Geology 33, 243–246.
John, T., Schenk, V., Mezger, K., Tembo, F., 2004. Timing and PT evolution of whiteschist metamorphism in the Lufilian Arc–Zambezi Belt Orogen (Zambia): implications for the assembly of Gondwana. J. Geol. 112, 71–90.
Johnson, S.P., De Waele, B., Evans, D., Banda, W., Tembo, F., Milton, J.A., Tani, K., 2007. Geochronology of the Zambezi supracrustal sequence, southern Zambia: a record of Neoproterozoic divergent processes along the southern margin of the Congo Craton. J. Geol. 115, 355–374.
Kamona, A.F., Lévêque, J., Friedrich, G., Haack, U., 1999. Lead isotopes of the carbonate-hosted Kabwe, Tsumeb, and Kipushi Pb–Zn–Cu sulphide deposits in relation to Pan African orogenesis in the Damaran–Lufilian Fold Belt of Central Africa. Mineral. Deposita 34, 273–283.
Kampunzu, A.B., Cailteux, J.L.H., Kamona, A.F., Intiomale, M.M., Melcher, F., 2009. Sediment-hosted Zn–Pb–Cu deposits in the Central African Copperbelt. Ore Geol. Rev. 35, 263–297.
Key, R.M., Liyungu, A.K., Njamu, F.M., Somwe, V., Banda, J., Mosley, P.N., Armstrong, P.A., 2001. The western arm of the Lufilian Arc in NW Zambia and its potential for copper mineralization. J. Afr. Earth Sci. 33, 503–528.
Ludwig, K.R., 2001. Isoplot/Ex Version 2.49. A Geochronological Toolkit for Microsoft Excel. Berkeley Geochronology Center, Special Publication vol. 1a, pp. 1–55.
Luvizotto, G.L., Zack, T., Meyer, H.P., Ludwig, T., Triebold, S., Kronz, A., Münker, C., Stockli, D.F., Prowatke, S., Klemme, S., Jacob, D.E., von Eynatten, H., 2009. Rutile crystals as potential trace element and isotope mineral standards for microanalysis. Chem. Geol. 261, 346–369.
Machel, H.G., 2001. Bacterial and thermochemical sulfate reduction in diagenetic settings — old and new insights. Sediment. Geol. 140, 143–175.
Master, S., Rainaud, C., Armstrong, R.A., Phillips, D., Robb, L.J., 2005. Provenance ages of the Neoproterozoic Katanga Supergroup (Central African Copperbelt), with implications for basin evolution. J. Afr. Earth Sci. 42, 41–60.
McGowan, R.R., Roberts, S., Foster, R.P., Boyce, A.J., Coller, D., 2003. Origin of the copper-cobalt deposits of the Zambian Copperbelt: an epigenetic view from Nchanga. Geology 31, 497–500.
McGowan, R.R., Roberts, S., Boyce, A.J., 2006. Origin of the Nchanga copper–cobalt deposits of the Zambian Copperbelt. Mineral. Deposita 40, 617–638.
Meinhold, G., Anders, B., Kostopoulos, D., Reischmann, T., 2008. Rutile chemistry and thermometry as provenance indicator: an example from Chios Island, Greece. Sediment. Geol. 203, 98–111.
Meneghel, L., 1981. The occurrence of uranium in the Katanga System of northwestern Zambia. Econ. Geol. 76, 56–68.
Muchez, P., Corbella, M., 2012. Factors controlling the precipitation of copper and cobalt minerals in sediment-hosted ore deposits: advances and restrictions. J. Geochem. Explor. 118, 38–46.
Muchez, P., Vanderhaeghen, P., El Desouky, H., Schneider, J., Boyce, A., Dewaele, S., Cailteux, J.L.H., 2008. Anhydrite pseudomorphs and the origin of stratiform Cu–Co ores in the Katangan Copperbelt (Democratic Republic of Congo). Mineral. Deposita 43, 575–589.
Muchez, P., André-Mayer, A.S., El Desouky, H.A., Reisberg, L., 2015. Diagenetic origin and multiphase modification of world-class Cu–Co deposits in the Central African Copperbelt. Mineral. Deposita 50, 437–447.
Nowecki, J. (2014). Tracing Seawater Evaporation and Its Role in the Formation of Sediment-hosted Stratiform Copper Deposits. Unpublished PhD thesis, University of Southampton, 217 pp.
Paquette, J.L., Tiepolo, M., 2007. High resolution (5 μm) U–Th–Pb isotope dating of monazite with excimer laser ablation (ELA)-ICPMS. Chem. Geol. 240, 222–237.
Paton, C., Hellstrom, J., Paul, B., Woodhead, J., Hergt, J., 2011. Iolite: freeware for the visualisation and processing of mass spectrometer data. J. Anal. At. Spectrom. 26, 2508–2518.
Pearce, N.J.G., Perkins, W.T., Westgate, J.A., Gorton, M.P., Jackson, S.E., Neal, C.R., Chenery, S.P., 1997. A compilation of new and published major and trace element data for NIST SRM 610 and NIST SRM 612 glass reference materials. Geostand. Newslett. 21, 115–144.
Poitrasson, F., Chenery, S., Shepherd, T.J., 2000. Electron microprobe and LA-ICP-MS study of monazite hydrothermal alteration: implications for U–Th–Pb geochronology and nuclear ceramics. Geochim. Cosmochim. Acta 64, 3283–3297.
Porada, H., Berhorst, V., 2000. Towards a new understanding of the Neoproterozoic–Early Palaezoic Lufilian and northern Zambezi Belts in Zambia and the Democratic Republic of Congo. J. Afr. Earth Sci. 30 (3), 727–771.
Richards, J.P., Krogh, T.E., Spooner, E.T.C., 1988a. Fluid inclusion characteristics and U-Pb rutile age of late hydrothermal alteration and veining at the Musoshi stratiform copper deposit, Central African Copperbelt, Zaire. Econ. Geol. 83, 118–139.
Richards, J.P., Cumming, G.L., Krstic, D., Wagner, P.A., Spooner, E.T.C., 1988b. Pb isotope constraints on the age of sulfide ore deposition and U–Pb age of late uraninite veining at the Musoshi stratiform copper deposit, Central Africa Copperbelt, Zaire. Econ. Geol. 83, 724–741.
Rose, D., 1980. Brabantite, $CaTh(PO_4)_2$, a new mineral of the monazite group. N. Jb. Mineral. Mh. 6, 247–257.
Selley, D., Broughton, D., Scott, R., Hitzman, M., Bull, S.W., Large, R.R., McGoldrick, P.J., Croaker, M., Pollington, N., Barra, F., 2005. A new look at the geology of the Zambian Copperbelt. Economic Geology 100th Anniversary Volume, pp. 965–1000.
Spear, F.S., Pyle, J.M., 2002. Apatite, monazite, and xenotime in metamorphic rocks. Rev. Mineral. Geochem. 48, 293–335.
Steven, N., Armstrong, R., 2003. A metamorphosed Proterozoic carbonaceous shale-hosted Co–Ni–Cu deposit at Kalumbila, Kabompo Dome: the Copperbelt ore shale in northwestern Zambia. Econ. Geol. 98, 893–909.
Sweeney, M.A., Binda, P.L., 1994. Some constraints on the formation of the Zambian Copperbelt deposits. J. Afr. Earth Sci. 19 (4), 303–313.
Torrealday, H.I., Hitzman, M.W., Stein, H.J., Markley, R.J., Armstrong, R., Broughton, D., 2000. Re–Os and U–Pb dating of the vein-hosted mineralization at the Kansanshi copper deposit, Northern Zambia. Econ. Geol. 95, 1165–1170.
Torremans, K., Gauquie, J., Boyce, A.J., Barrie, C.D., Dewaele, S., Sikazwe, O., Muchez, P., 2013. Remobilisation features and structural control on ore grade distribution at the Konkola stratiform Cu–Co ore deposit, Zambia. J. Afr. Earth Sci. 79, 10–23.
Triebold, S., von Eynatten, H., Luvizotto, G.L., Zack, T., 2007. Deducing source rock lithology from detrital rutile geochemistry: an example from the Erzgebirge, Germany. Chem. Geol. 244, 421–436.
Unrug, R., 1983. The Lufilian Arc: a microplate in the Pan-African collision zone of the Congo and the Kalahari cratons. Precambrian Res. 21, 181–196.
Vanderhaeghe, O., 2012. The thermal–mechanical evolution of crustal orogenic belts at convergent plate boundaries: a reappraisal of the orogenic cycle. J. Geodyn. 56–57, 124–125.
Zack, T., Moraes, R., Kronz, A., 2004a. Temperature dependence of Zr in rutile: empirical calibration of a rutile thermometer. Contrib. Mineral. Petrol. 148, 471–488.
Zack, T., von Eynatten, H., Kronz, A., 2004b. Rutile geochemistry and its potential use in quantitative provenance studies. Sediment. Geol. 171, 37–58.